The Thesis Committee for Ellen Katherine Wilkes
Certifies that this is the approved version of the following thesis:

The Effect of Channel Parameters on the Adiabatic Film Cooling Effectiveness of Shaped Holes in Crossflow

APPROVED BY
SUPERVISING COMMITTEE:

Supervisor:

David G. Bogard

Michael E. Webber

The Effect of Channel Parameters on the Adiabatic Film Cooling Effectiveness of Shaped Holes in Crossflow

by

Ellen Katherine Wilkes, B.S.M.E.

Thesis

Presented to the Faculty of the Graduate School of

The University of Texas at Austin

in Partial Fulfillment

of the Requirements

for the Degree of

Master of Science in Engineering

The University of Texas at Austin

December 2015

Dedication

I would like to dedicate this thesis to my parents - who I love very much and who let me live in their house and eat all their food for free for the past year and half – and my fiancé - for his love and support and agreeing to marry me.

Acknowledgements

I would like to first thank Dr. David Bogard for his guidance and encouragement throughout graduate school. I also want to thank the members of the TTCRL – Kyle Chavez, Josh Anderson, John McClintic, Gavin Packard, Adam Vaclavik, Brad Keiser, Khanh Hoang, Daniel Goodwin, Michelle Prichard, Christopher Yoon, Theo Ribadeneyra, and Jabob Moore – for teaching me how to do science and for being the best group of people ever.

Abstract

The Effect of Channel Parameters on the Adiabatic Film Cooling Effectiveness of Shaped Holes in Crossflow

Ellen Katherine Wilkes, M.S.E.

The University of Texas at Austin, 2015

Supervisor: David G. Bogard

There is limited information in the literature on the behavior of shaped film cooling holes fed by crossflow and even less information on the effect of crossflow parameters on film cooling performance. Here, two scaled film cooling models were used to independently vary the crossflow Reynolds numbers in the range of 36,000 to 57,000 and the crossflow velocity ratio from 0.36 to 0.64. Careful attention was paid to controlling physical parameters between comparisons to isolate the effects of internal velocity ratio or Reynolds number on the performance of shaped holes. In the process of controlling the physical parameters of the system, a novel correction for coolant to mainstream density ratio was proposed. The results of this study showed that channel velocity ratio had a larger effect on the film cooling performance of shaped holes than channel Reynolds number. When the mass flux of fluid through the film cooling holes was at the highest and lowest value, increasing the channel velocity ratio decreased the film cooling effectiveness. At a middle mass flux, the outcome was opposite such that an increase in channel velocity ratio resulted in increased effectiveness.

Table of Contents

List of Tables

List of Figures

Introduction

Gas turbines are an integral part of today's society: generating power, propelling marine equipment, providing thrust for aeronautical applications and driving industrial machinery such as compressors and pumps. In a nutshell, a gas turbine is a combustion engine used to produce a net work output. A simplified model of gas turbine engine operation is the Brayton Cycle, shown graphically and schematically in Figure 1. In the Brayton cycle, fluid is compressed in the compressor (stages 1-2), heated in the combustor (stages 2-3), expanded in the turbine (stages 3-4), and then expelled to atmosphere (stage 4). Work is generated by the expansion of gas in the turbine. Part of this generated work is used to compress gas in the compressor, but the excess work is the net work output and can be transformed into usable energy for other applications.

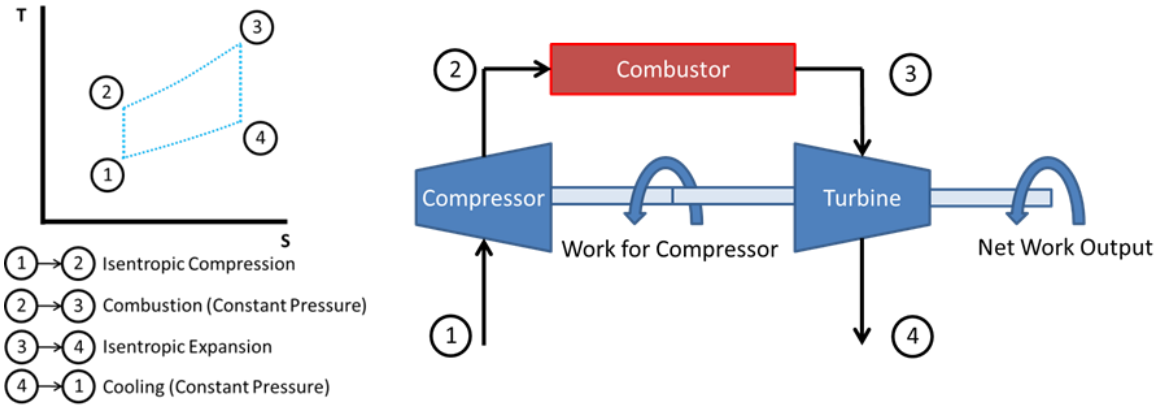

Figure 1: Graphic and schematic representation of the Brayton Cycle [1]

If the working fluid of the Brayton Cycle is a perfect gas and there is no heat loss or friction in the engine components, then the cycle can be termed an ideal Brayton Cycle. The efficiency of an ideal Brayton Cycle can be expressed in terms of

temperatures, as given in equation 1, where subscripts correspond to the stages shown in Figure 1 [2].

$$\eta_{th} = 1 - \frac{T_4 - T_1}{T_3 - T_2} \quad (1)$$

This equation shows that increasing T_3, the temperature of the gas exiting the combustor, increases the efficiency of the whole system. In actual engine design and manufacturing, the temperature exiting the combustor and entering the turbine is designed and operated at hotter and hotter temperatures. Although increasing T_3 does increase engine efficiency, these temperatures are so hot that they have exceeded the melting temperature of many of the engine components, specifically the first stage turbine blades and vanes. Consequently, developing more sophisticated cooling methods would avoid damage and help achieve higher performance. The three main methods of blade and vane cooling are thermal barrier coatings, internal cooling passages, and film cooling. Thermal barrier coating (TBC) is a low thermal conductivity material used to coat the entire component and insulate it from the hot mainstream gases. Internal cooling passages are pathways inside the turbine airfoil through which cooler air from the compressor stage is routed. The cooler air cools the airfoil material by convection, allowing the blade or vane to withstand higher mainstream temperatures. By installing rib turbulators, or systematic protrusions into the flow, within the passageways or changing the shape of the ducts, designers can increase the turbulence of the air through the passageways and increase the heat transfer of heat from the airfoil [3].

Film cooling is a method that pulls cooler air from the compressor stage through cooling passages inside the airfoil and out through cooling holes on the surface of the

airfoil, as shown in Figure 2. The coolant flowing out of the surface cooling holes creates a protective barrier from the oncoming hot mainstream gas. Film cooling works in conjunction with internal cooling since the film cooling holes are fed by internal cooling passages, but the term film cooling generally focuses on the external aspect of cooling.

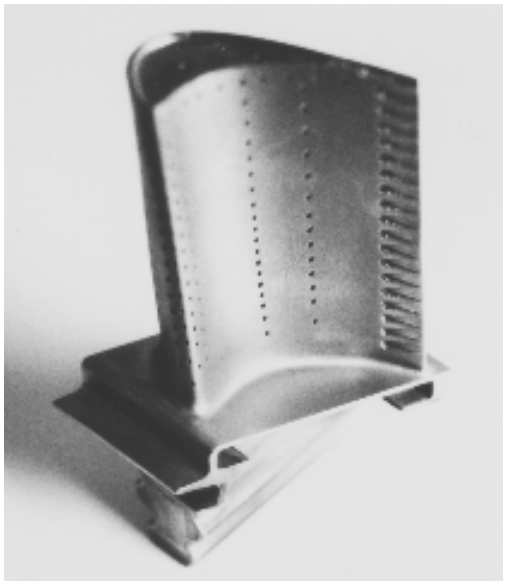

Figure 2: Image of engine airfoil with film cooling holes [4]

This thesis focuses on film cooling as a method for cooling turbine airfoils. Laboratory film cooling experiments are important for industry because actual engine conditions are too hot, too small, and too fast to take accurate film cooling measurements. In laboratories, scaled up models of turbine airfoils and film cooling holes are tested in stationary test sections at around room temperature. Dimensionless physical parameters of the laboratory tests are matched to the parameters of actual engine conditions so that the laboratory results can be applied to engine design. One of these key parameters is coolant to mainstream density ratio. In engine conditions, the mainstream is very hot

while the coolant is cooler and denser, resulting in density ratios around $DR = 2.0$. To produce this same density ratio in laboratory conditions with room temperature mainstream, a colder and denser coolant is used. In this study, liquid nitrogen is used to cool air to the appropriate temperature. Density ratio is generally a key dimensionless parameter but generally considered to have a weak effect on the performance of film cooling. This thesis proposes a correlation to correct for this weak effect of density ratio.

There are hundreds of studies that investigate film cooling, most of which either use a plenum to feed coolant to the film cooling holes on a flat plate or use a scaled airfoil model with film cooling holes fed by internal passages. However, a plenum coolant feed, although able to isolate the external film cooling effects from the internal effects, is not indicative of the internal passageways used to feed film cooling holes in actual engine conditions and the studies using a scaled airfoil model do not monitor the parameters of the internal flow. There are several studies that investigate the effect of coolant crossflow on the performance of cylindrical film cooling holes, but there are only eight studies in the current literature [5], [6], [7], [8], [9], [10], [11], [12] that look at the effect of crossflow coolant feed on shaped film cooling holes. These six studies look at the effect of crossflow on film cooling performance, but do not consider the effect of the crossflow parameters. Two of the studies examine the effect of internal Mach number on film cooling effectiveness, but do not isolate the internal Mach number from internal Reynolds number or internal velocity ratio. This thesis aims to fill this gap in the literature by studying the effect of two coolant crossflow parameters, velocity ratio and Reynolds number, on the film cooling performance of shaped holes.

Background

The performance of film cooling is quantified by a parameter called adiabatic effectiveness, η. Adiabatic effectiveness characterizes how well coolant from the film cooling holes cools an adiabatic surface. Adiabatic effectiveness is defined as:

$$\eta = \frac{T_\infty - T_{aw}}{T_\infty - T_{c,exit}} \tag{2}$$

Where T_∞ is the mainstream gas temperature, T_{aw} is the adiabatic wall temperature, and $T_{c,exit}$ is the coolant temperature exiting the cooling holes. If T_{aw} equals the exit coolant temperature, then there is 100% effectiveness but if the wall temperature equals T_∞, then there is 0% effectiveness. T_{aw} is the temperature of the gas in contact with the wall and is generally taken to be the driving temperature for heat transfer, shown in Figure 3a. T_{aw} is expected to also be the driving temperature for heat transfer on a conducting airfoil at the edge of the thermal boundary layer, shown in Figure 3b. T_{aw} and h_f are used as boundary conditions in analysis of the heat transfer in the solid to determine T_w of an actual blade or vane model.

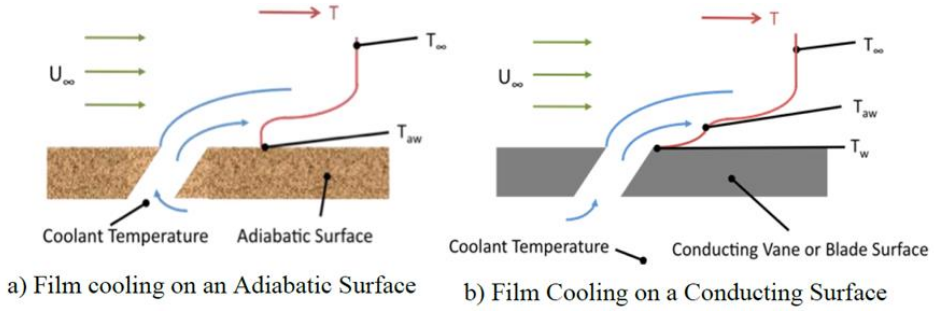

Figure 3: a) Film cooling and thermal profile on adiabatic surface and b) Film cooling and thermal profile on a conducting surface [13]

There is, however, a second part to quantifying the effectiveness of film cooling. In reality, the presence of film cooling jets can actually increase the heat transfer from the mainstream to the wall because of increased turbulence created by the jets mixing with the mainstream flow. A metric termed heat transfer coefficient augmentation can be used to quantify this increase in heat transfer to the wall, denoted as h_f/h_0, where h_f is the heat transfer coefficient with film cooling and h_0 is the heat transfer coefficient without film cooling. h_f is determined by experimentally measuring adiabatic wall temperature and wall temperature and back-calculating the heat transfer coefficient using a known heat flux from:

$$q'' = h_f(T_{aw} - T_w) \tag{3}$$

Where q'' is the heat flux entering the surface, T_{aw} is the temperature of the adiabatic wall, and T_w is the temperature of the wall. The heat transfer coefficient without film cooling, h_0, is found by similar means using equation 4.

$$h_0 = \frac{q''}{T_\infty - T_w} \tag{4}$$

Where q'' is the heat flux entering the surface, T_∞ is the temperature of the mainstream, and T_w is the temperature of the wall. Results from Boyd [13], a study using the same hole geometry tested in this thesis, found that for shaped holes fed by a plenum at DR = 1.5 the heat transfer coefficient augmentation is around 1.0, increasing up to 1.07 for higher blowing ratios. However, there is no data in the literature that looks at the heat

transfer coefficient augmentation for shaped holes fed by cross-flow, and so for purposes of this study the heat transfer coefficient augmentation was assumed to be approximately one. A heat transfer coefficient augmentation of one means that the increase in heat transfer to the wall due to the film cooling jets is negligible and adiabatic effectiveness is a sufficient measure of the film cooling performance.

Film cooling holes are generally cylindrical or shaped in geometry. Shaped holes have a diffuser at the exit of the cooling hole and are designed to diffuse the flow before the coolant jet comes in contact with the mainstream. Flowfield measurements for cylindrical holes and shaped holes fed by a co-flow, which is a coolant feed that flows parallel to the mainstream flow, performed by Thole et al. [14], show that the diffuser of the shaped hole produces the anticipated cooling effects. The three cooling hole geometries used in [14] are shown in Figure 4. Velocity vectors of the jets issuing into the mainstream show that there is greater and sooner mainstream penetration for cylindrical holes than with either lateral expanded holes or forward-lateral expanded holes. Between the lateral expanded and forward-lateral expanded cooling holes, the presence of the forward expansion causes even less jet penetration into the mainstream, allowing the coolant to remain better attached to the wall.

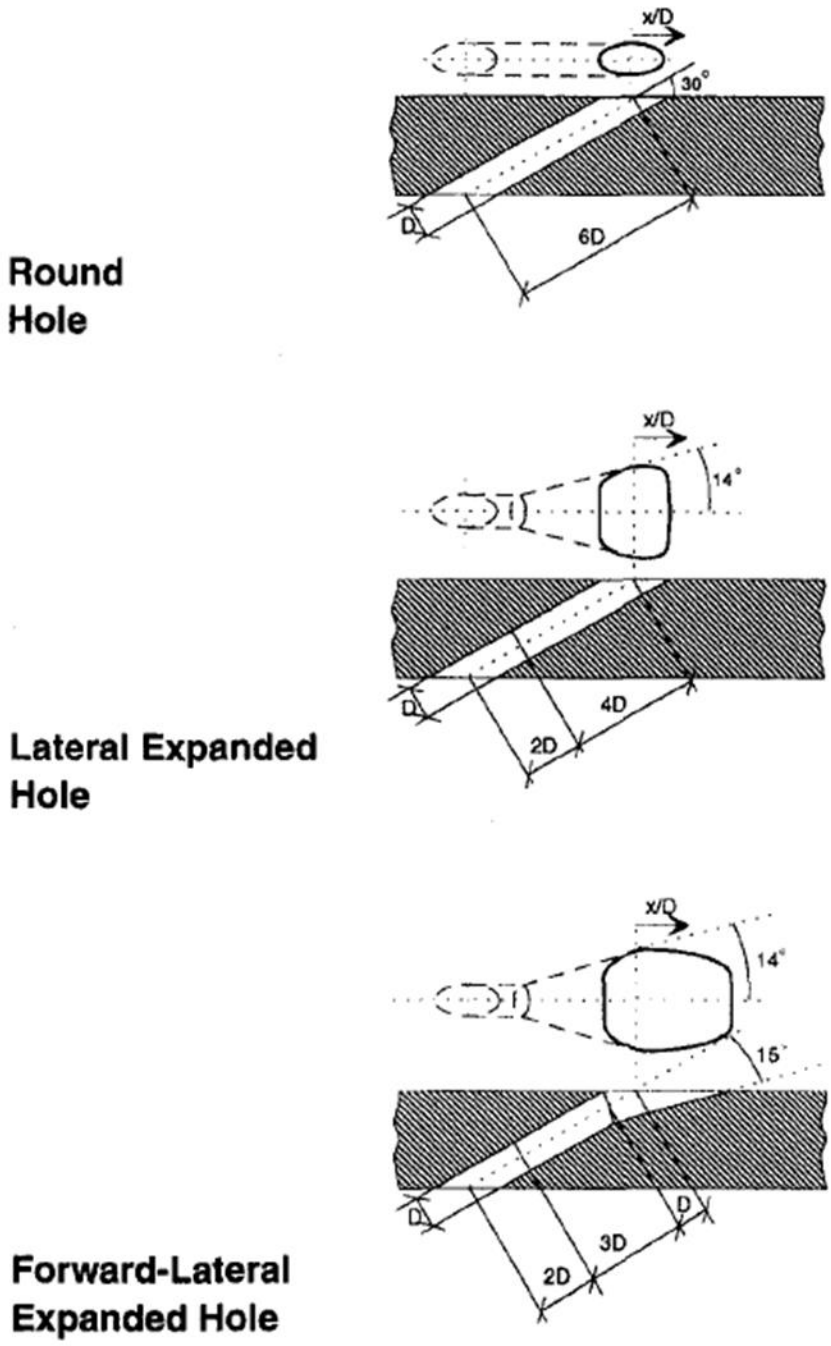

Figure 4: Example of film cooling geometries [14]

Gritsch et al. [7] also studied three hole geometries fed by a parallel coolant supply – cylindrical, fan-shaped, and laidback fan-shaped cooling holes – but with different dimensions than [14]. Cylindrical holes had peak adiabatic effectiveness at a blowing ratio, a ratio of the mass flux of fluid through the cooling holes to the mainstream, of $M = 0.5$ and jet separation from the wall by $M = 1.0$. This jet separation resulted in reduced effectiveness at the wall and, therefore, was detrimental to film cooling. The fan-shaped hole had improved lateral spreading compared to the cylindrical hole, but majority of the effectiveness was still along the centerline of the jet. The laidback fan-shaped hole had slightly less effectiveness along the jet centerline, but improved lateral spreading resulted in increased off-center effectiveness. Neither the fan-shaped or laidback fan-shaped holes showed signs of jet separation up to $M = 1.5$. Even though shaped holes exhibit improved film cooling characteristics than cylindrical holes, they are considerably more expensive to machine into engine parts, and for this reason, a combination of shaped and cylindrical holes are used in film cooling configurations.

As previously discussed, many flat plate experiments are conducted using a plenum to feed coolant to the coolant holes, but this type of coolant feed is not representative of actual engine conditions. To simulate actual engine conditions where the coolant flows through passageways perpendicular to the mainstream, a cross-flow coolant feed is used for the experiments in this thesis. The presence of cross-flow with an internal Mach number $Ma_c = 0.3$ and a mainstream Mach number of $Ma_\infty = 0.3$ was found by Saumweber and Schulz [9] to increase the adiabatic effectiveness for cylindrical holes by on average $\eta = 0.05$ and decrease the effectiveness for shaped holes by about $\eta = 0.1$ when compared to plenum fed conditions, though these values varied depending on blowing ratio and position downstream of the cooling holes. Although the effectiveness

of shaped holes was decreased with an inlet cross-flow, shaped holes fed by cross-flow still performed better than cylindrical holes fed by cross-flow for the blowing ratios tested. Shaped holes and cylindrical holes have similar performance at low blowing ratios, but shaped holes perform better than cylindrical holes at higher blowing ratios since the cylindrical holes are more prone to jet separation leading to decreased effectiveness. The results also showed that for cylindrical holes, the presence of crossflow increased the lateral spreading of the jet and reduced the tendency of the jet to separate at higher blowing ratios. For shaped holes, cross-flow coolant feed results in an asymmetric and 11% widened coolant footprint with shorter downstream coverage. These findings on the effect of cross-flow for shaped holes and cylindrical holes are confirmed by the results in several other studies [10], [6], and [8]. Designers rely heavily on experimental methods to study the properties and effectiveness of film cooling because computational fluid dynamics has difficulty predicting film cooling with accuracy, however, the method gives good insight into the trends of different film cooling conditions. A computational study by Kohli and Thole [5] investigated the in-hole effects of coolant cross-flow for both cylindrical and laidback fan shaped holes. In comparing the in-hole velocity vectors for cylindrical holes, the plenum fed holes showed the formation of a counter rotating vortex pair (CRVP) as the jet moves through the hole, while the cross-flow fed hole shows a single off-center vortex. The single off-center vortex is indicative of a helical motion as the flow moves through the hole. Looking at shaped holes a CRVP forms at the inlet to the plenum fed hole, but is disrupted by the expansion of the shaped hole at the exit plane. For the shaped hole fed by cross-flow, there is no CRVP but a single off-center vortex that swirls its way through the hole until it is disrupted by the diffuser.

Multiple studies have shown that there is an effect of coolant cross-flow on film cooling. Few of these studies, though, have looked into what effect cross-flow parameters have on film cooling. Saumweber and Schulz [9] studied the effect of cross-flow Mach number from Ma_c = 0.1 to 0.6 on cylindrical and shaped holes and concluded that increasing internal Mach number leads to greater skewing of the jet and a slightly wider jet footprint, less than 5 % increase in width, resulting from stronger helical motion inside the coolant hole. For cylindrical holes at low cross-flow velocities, the jets were more prone to detachment from the wall resulting in lowered adiabatic effectiveness. These Mach number comparisons were performed at a constant blowing ratio of M = 1.0 but without holding the channel velocity ratio or channel Reynolds number constant. Saumweber et al. [10] also looked into the effect of internal Mach number for shaped holes and found that increased channel Mach number resulted in a decreased discharge coefficient but, like [9], neglected to isolate these effects from internal velocity ratio or Reynolds number.

Examination of the literature shows not only the need for additional studies on the effect of crossflow on shaped film cooling holes and particularly studies of the effect of crossflow parameters on film cooling, but also the need for systematic parameter control. This thesis studies the effect of internal velocity ratio and internal Reynolds number on the performance of shaped film cooling holes by using two scaled film cooling models to vary internal velocity ratio and internal Reynolds number independently of each other. A comparison of the crossflow fed holes to plenum fed holes is also presented for reference. This study pays particular attention to holding the experimental parameters constant between comparisons so as to isolate the effect of the parameters of interest.

Experimental Methods

This chapter is broken up into seven sections. The first two sections, Experimental Setup and Temperatures Measurements, focus on the experimental facility and measurement techniques. The third and fourth sections, Design of Operational Parameters and Density Ratio Correction, discuss the operational parameters of the experiments including how and why they were designed and the correction of density ratio made to systematically control the operational parameters. The fifth section, Conduction Correction, presents the correction made to the measured wall temperatures to correct out conduction errors through the coupon material. The sixth section, Testing of the 4x Scale Model, focuses on the difficulties of testing the 4x scale film cooling model and the solutions generated to reduce those issues. The last section, Uncertainty Analysis and Repeatability discusses the uncertainty in the operational parameters and adiabatic effectiveness measurements and how these values were determined.

EXPERIMENTAL SETUP

The purpose of this study was to investigate the effect of internal velocity ratio and Reynolds number on the adiabatic effectiveness of shaped holes in cross-flow. Two scaled film cooling models, a 4x scale and an 8x scale, were tested to independently vary channel Reynolds number and channel velocity ratio. For reference, the channel results were compared to results using the same hole geometry but fed by a plenum, whose operational parameters are denoted as Test 1 in Table 1. The operational parameters for all experiments run for this study are shown in Table 1, where d is the coolant hole diameter, DR is the coolant to mainstream density ratio, U_∞ is the velocity of the tunnel

mainstream, Ma_∞ is the mainstream Mach number, $Re_{\infty,d}$ is the mainstream Reynolds number based on coolant hole diameter, δ^*/d is the boundary displacement thickness with respect to coolant hole diameter, Re_{ch} is the Reynolds number through the coolant channel, and VR_{ch} is the coolant channel to mainstream velocity ratio. Test 2 and Test 3 were compared to show the effect of channel Reynolds number while keeping channel velocity ratio nominally constant. Test 2 and 4 were compared to show the effect of channel velocity ratio while keeping channel Reynolds number constant. A further discussion of the parameters of the experiments is presented later in this section.

Table 1: Operational parameters for experiments

Parameter	**1**	**2**	**3**	**4**
Scale Factor	18x	8x	4x	4x
Coolant Feed	Plenum	Channel	Channel	Channel
d	9 mm	4 mm	1.8375 mm	1.8375 mm
DR	1.8	1.8	1.5	1.5
U_∞	10.5 m/s	25 m/s	54 m/s	54 m/s
Ma_∞	0.03	0.07	0.15	0.15
$Re_{\infty,d}$	5,500	6,011	6,011	6,011
δ^*/d	0.29	0.31	0.35	0.35
Re_{ch}	N/A	57,000	38,000	57,000
VR_{ch}	N/A	0.36	0.36	0.64

The mainstream velocity for Test 3 and 4 was U_∞ = 54 m/s. The wind tunnel and test section, that previously had a maximum velocity of U_∞ = 20 m/s, was rebuilt to operate at these higher mainstream velocities and Mach numbers. This wind tunnel facility, located in the Turbulence and Turbine Cooling Research Laboratory at The University of Texas at Austin, was remodeled to be a low speed, closed loop wind tunnel powered by a 30 hp motor. The mainstream flow was directed into a 152 mm high by 610

mm wide test section, shown in Figure 5 with the 8x scale test coupon installed and in Figure 6 with the 4x scale test coupon installed, where adiabatic effectiveness measurements of the shaped coolant holes were taken. A passive turbulence generator was installed upstream of the coolant holes to generate isotropic turbulence. The test section was designed such that the turbulence generator could be installed in any of three slots, as shown in Figure 7, at different distances upstream of the cooling holes to produce the desired turbulence. The turbulence generator, shown in Figure 8, was made up of a series of vertical cylindrical aluminum rods 10 mm in diameter spaced evenly 35 mm apart across the width of the test section. For the experiments in this study, the turbulence generator was installed in the farthest downstream slot to generate a laterally uniform turbulence intensity of Tu = 5.5% with an integral length scale of Λ = 10 mm measured by traversing a hotwire probe in the vertical plane at the hole breakout location. The integral length scale to hole diameter ratio was not kept constant from test to test and varied from Λ/d = 2.5 – 5.4.

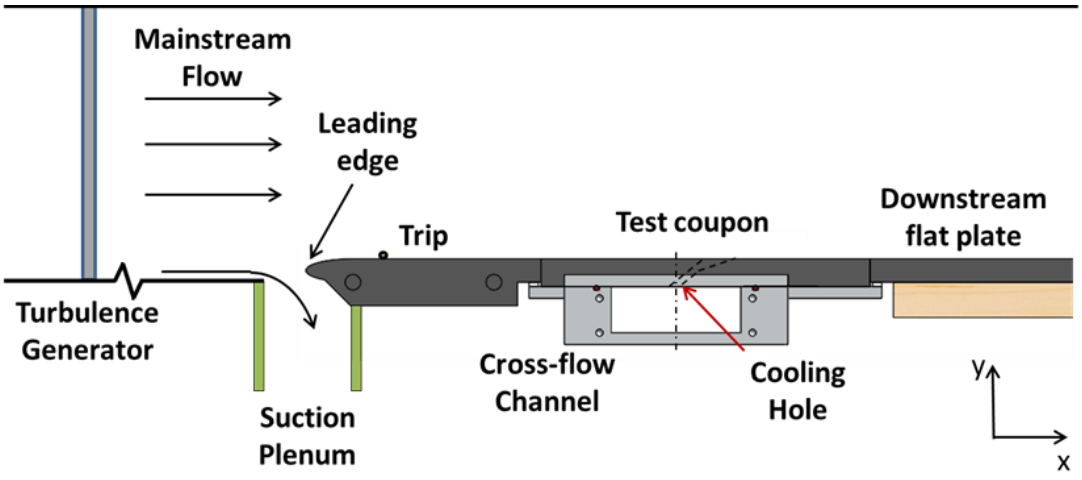

Figure 5: Schematic of wind tunnel test section with 8x scale test coupon and channel installed

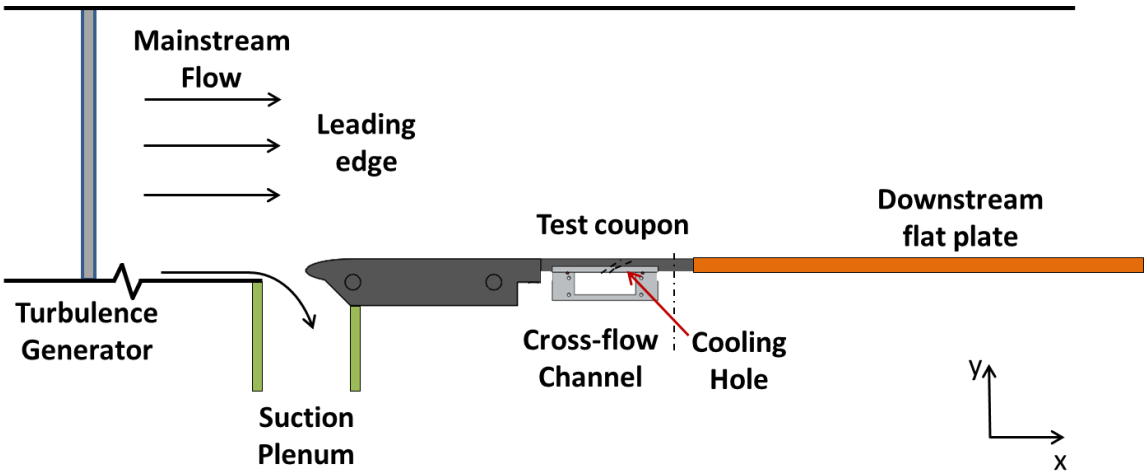

Figure 6: Schematic of wind tunnel test section with 4x scale test coupon and channel installed

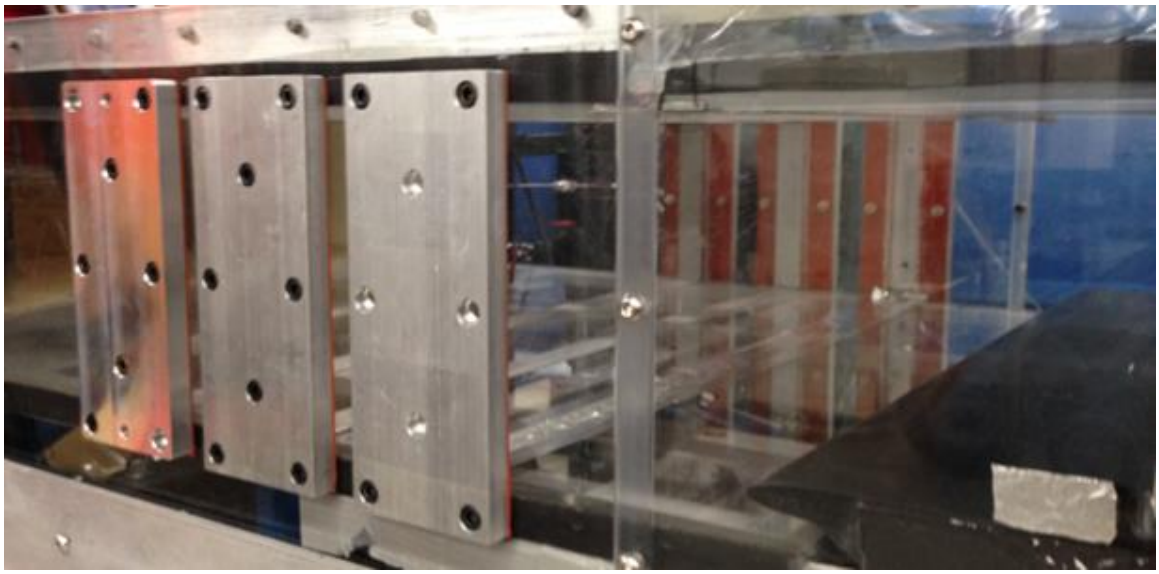

Figure 7: Turbulence generator slots at various distances upstream of the film cooling holes

Figure 8: Passive turbulence generator

A suction plenum was installed beneath the floor of the test section, as shown in Figures 5 and 6, upstream of the cooling holes to remove the upstream boundary layer such that a new boundary layer began to form at the stagnation point of the leading edge. The suction plenum was connected to the suction side of a 7.5 hp blower to obtain the appropriate pull through the suction slot in the test section. A cylindrical trip was fixed horizontally across the width of the test section to quicken the transition to a turbulent boundary layer. The diameter and placement of the trip was used to control the boundary layer at the location of the coolant holes and obtain the specified boundary layer thickness. The approach boundary layers for both the 8x and 4x scale conditions were measured by traversing a Preston tube across the height of the test section at the location of the holes without film cooling. The boundary layer thickness for the 8x scale case was measured to be δ = 11.5 mm, resulting in a δ/d = 2.88 and the boundary layer thickness for the 4x scale conditions was measured to be δ = 6 mm, resulting in a δ/d = 3.27. The boundary layer thicknesses for the 8x scale condition was chosen to match the boundary layer thickness to hole diameter ratio of the 4x scale condition. The boundary layer thickness for the 4x scale condition was set to the minimal boundary layer thickness

available without a trip, but because the cooling holes were small, this resulted in a relatively large δ/d. The approach boundary layer profiles for the 8x and 4x scale conditions are shown respectively in Figures 9 and 10. The shapes of the boundary layer profiles for both conditions matched well with the 1/7th power law, indicating that the boundary layers were fully turbulent. The 1/7th power law is not always an exact estimate for a turbulent boundary layer shape, but it is generally an appropriate comparison.

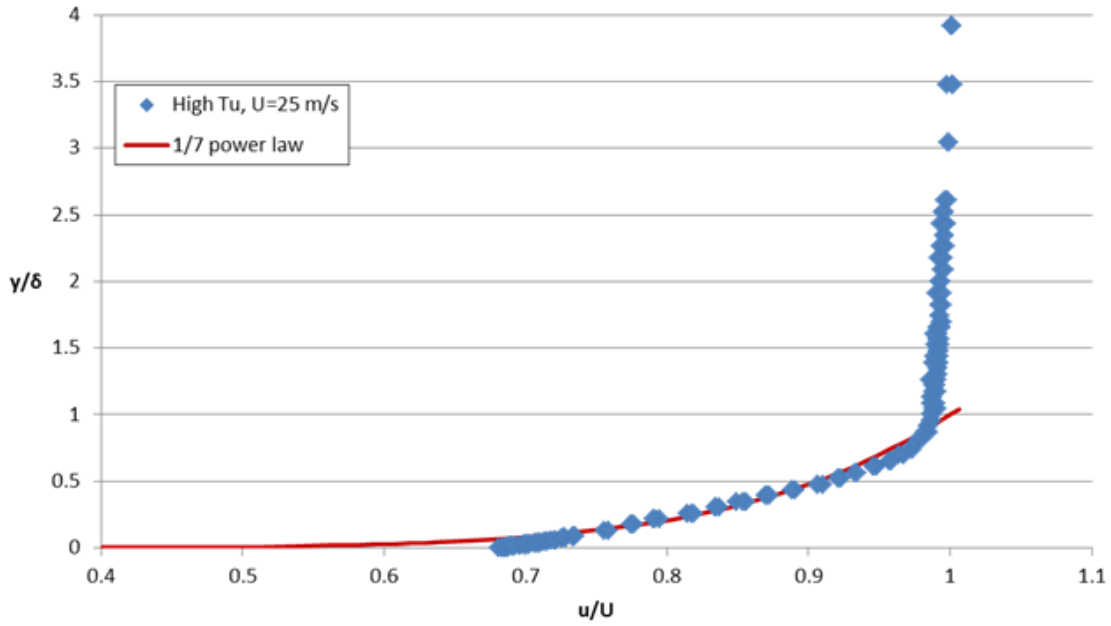

Figure 9: 8x scale approach flow boundary layer profile at the cooling hole location with U_∞ = 25 m/s

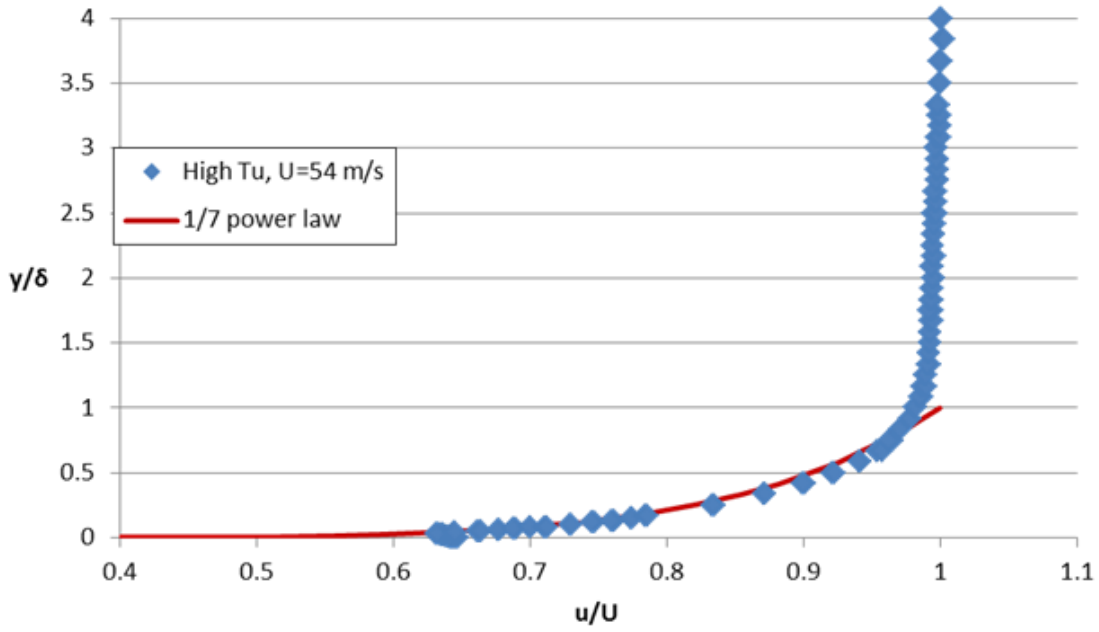

Figure 10: 4x scale approach flow boundary layer profile at the cooling hole location with U_∞ = 54 m/s

The test coupon was fixed in the test section downstream of the leading edge and housed the cooling hole geometry to be tested for each experiment. Two test coupons were constructed – one for the 8x scale cooling holes and one for the 4x scale cooling holes. The 8x scale coupon, presented in Figures 11 and 12, had a thickness of t = 12 mm and was constructed entirely of a closed cell, low thermal conductivity polyurethane foam (k ~ 0.048 W/mK). It was important that the coupon be made of a low conductivity material so that the measurements of the surface temperature during testing had as close to an adiabatic boundary condition at the wall as possible. The 4x scale coupon, shown in Figures 13 and 14, had a thickness of t = 5.5 mm and was made up of mostly chlorinated polyvinyl chloride (CPVC), which had a larger thermal conductivity than polyurethane

foam (k ~ 0.138 W/mK). Constructing the 4x scale coupon out of polyurethane foam would have been ideal, but the large cell structure of the foam made it difficult to machine the small coolant holes with accuracy, so a more uniform material with a slightly higher thermal conductivity was selected. To reduce the amount of heat transfer through the 4x scale coupon during testing, a 2.4 mm thick sheet of polyurethane foam was secured into a shallow pocket in the CPVC, starting 1.9 hole diameters downstream of the cooling hole exits. The foam sheet was secured into the pocket and sanded down until it was flush with the CPVC surface – particular attention was paid to the smoothness of the seam between the CPVC and foam directly downstream of the hole exits.

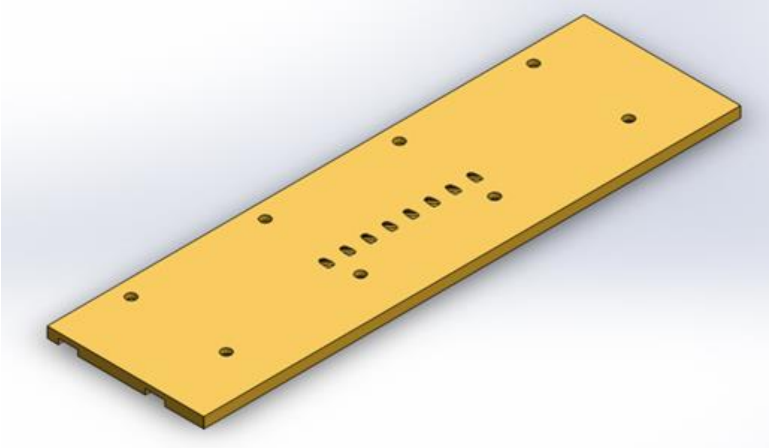

Figure 11: Model of the 8x scale polyurethane foam coupon

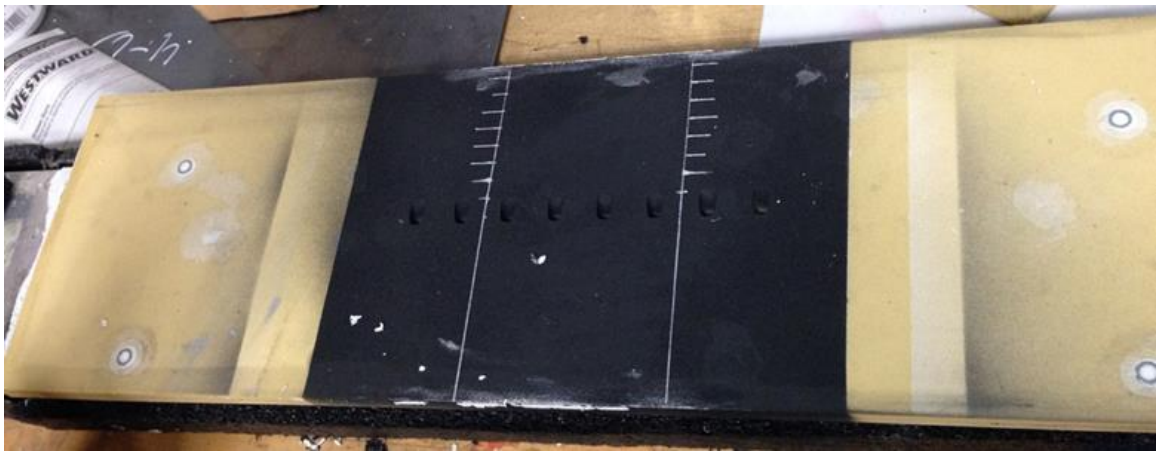

Figure 12: Photo of the 8x scale polyurethane foam coupon assembled to coolant channel

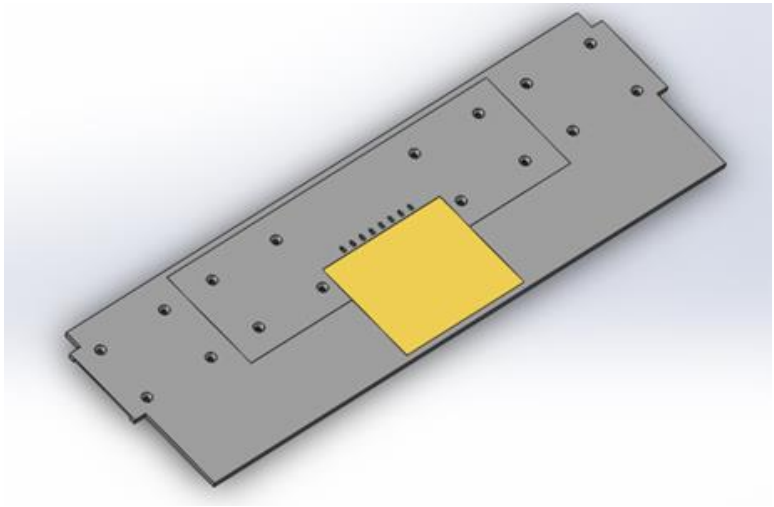

Figure 13: Model of the 4x scale CPVC and polyurethane foam coupon

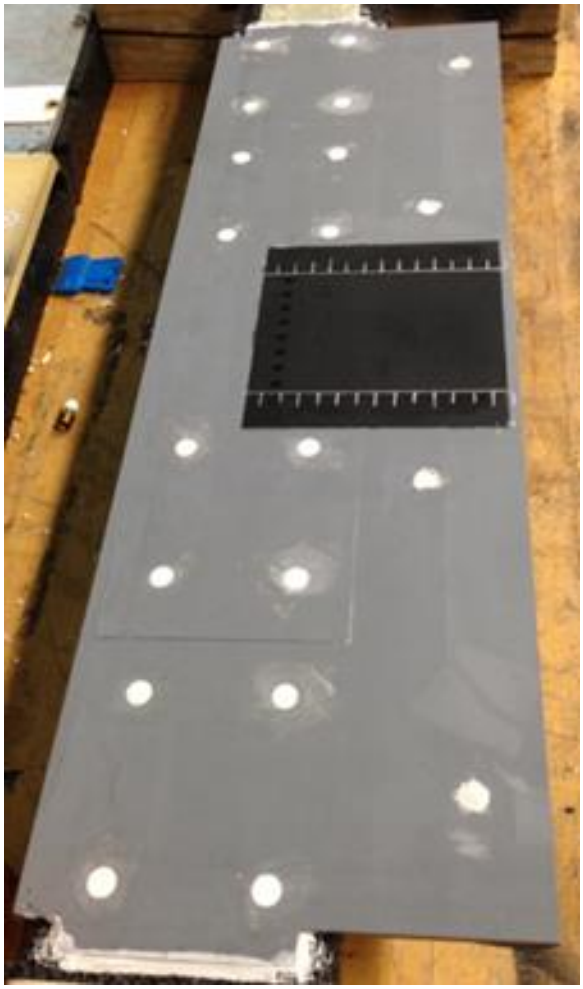

Figure 14: Photo of 4x scale CPVC and polyurethane foam coupon assembled to channel

Each coupon housed eight shaped film cooling holes. A laid-back fanshaped cooling hole – the 7-7-7 shaped hole - tested in this study was designed by Schroeder and Thole [15] to be an open-literature shaped film cooling hole representative of actual engine geometries. The 8x scale cooling hole had a diameter of d = 4.0 mm, while the 4x scale cooling hole had a diameter of d = 1.84 mm. The hole diameters were not a factor

of 2 different, but for ease of identification, they were labeled as 4x and 8x scale models. The holes, depicted in Figure 15, were machined with a lateral expansion angle of $\beta = 7°$, with a forward expansion angle of $\delta = 7°$ and at an injection angle of $\alpha = 30°$.

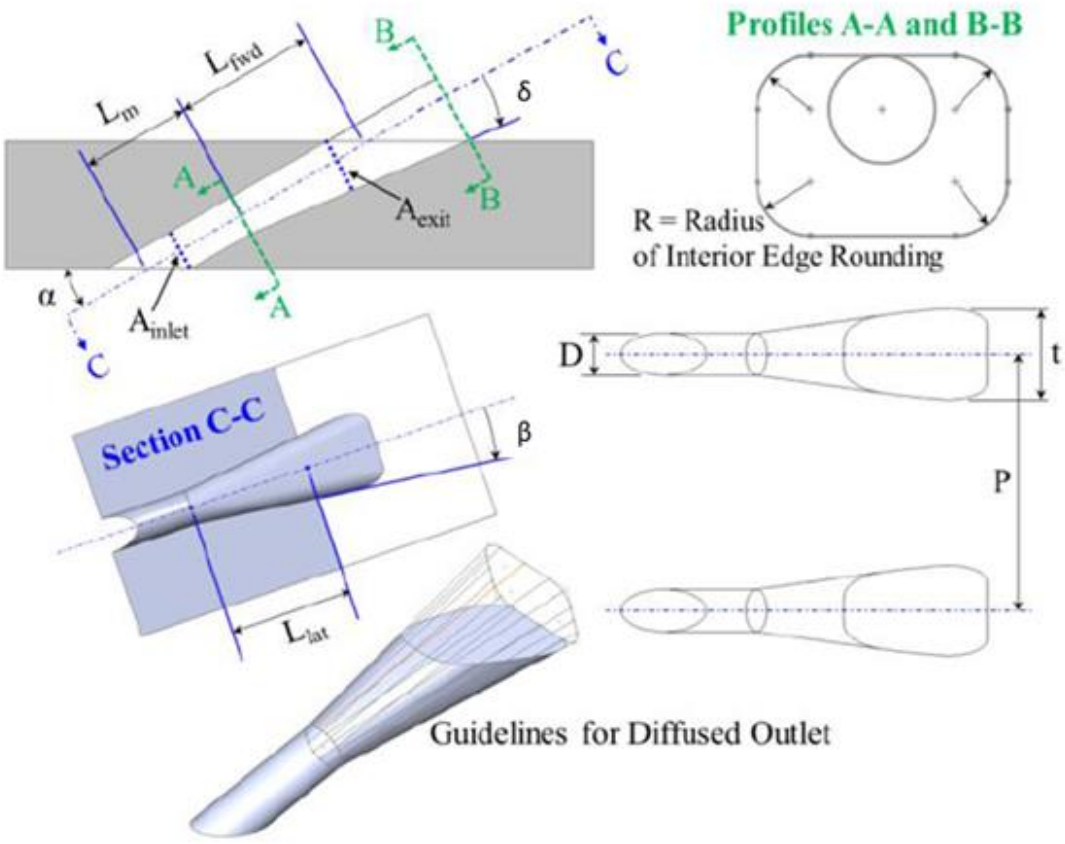

Figure 15: 7-7-7 shaped film cooling hole geometry [15]

Both cooling holes had a length of $l/d = 6$ but different pitch spacing between the holes. Mistakenly, the 8x scale holes were spaced at a $p/d = 6$ while the 4x scale holes were spaced at a $p/d = 6.25$. Fortunately, this difference in pitch spacing was easily accounted for. Pitch, or hole spacing, was found by Schmidt et al. [16] to scale linearly

with laterally averaged effectiveness granted there was no interaction between the jets – a doubling in pitch spacing resulted in half the laterally averaged effectiveness. Since there was no interaction between jets in this study, a superposition approach was taken to correct out the difference in spacing between holes. Equation 5 was applied to the laterally averaged results of the 4x scale holes to compare to data with a pitch spacing of $p/d = 6$. The contour plots and lateral profiles of the 4x scale data were not corrected for the difference in pitch spacing.

$$\eta_1 = \eta_2 \left(\frac{p_2}{p_1}\right) \tag{5}$$

The cooling holes in the test coupon were fed coolant by a cross-flow channel positioned beneath the test coupon and used to simulate the effect of flow through coolant passageways in an airfoil. A different channel was used for the 8x scale model and the 4x scale model, the dimensions of which are given in Table 2. The channels were designed for 5 mm cooling holes and 1.84 mm cooling holes. Due to availability of test coupons, the final hole diameters were chosen as 4mm and 1.84 mm, so the dimensions of the channel were not scaled exactly as the coolant hole diameters. Both channels were constructed of aluminum and had a similar design, depicted in Figure 16. The 8x scale channel was used in a previous study and is described in detail in Klavetter [17] and shown completely assembled in Figure 17. The 4x scale channel was a modular channel and was designed specifically for this study. The channel was made up of five aluminum pieces (a bottom piece, two side bars, and two top plates) that fit together as shown in Figure 18. The 8x scale channel was constructed form a u-channel and two top plates, which was much more difficult to machine. The 4x scale channel was not only easier to

machine, but the dimensions of the channel could easily be changed for future use. By replacing the two side bars with side bars of different widths or heights, the dimensions of the channel could be altered without reconstructing an entirely new channel. To seal the channel, 0.9 mm wide and 0.05 mm deep grooves were cut into the top and bottom of the side bars to create a face seal using lengths of 1/16" silicone O-ring. The test coupon fit on top of the channel in between the two top plates. O-ring grooves were cut into the tops of the top plates and side bars to seal against tabs on the side of the test coupon as shown in Figure 19.

Table 2: Dimensions of crossflow coolant channels

	8x Scaled Channel	**4x Scaled Channel**
H_{ch}	25 mm	9 mm
W_{ch}	70 mm	26 mm
d_H	37 mm	14 mm
L_{ch}	1680 mm	1276 mm
L_e	$10.35d_H$	$34.3d_H$

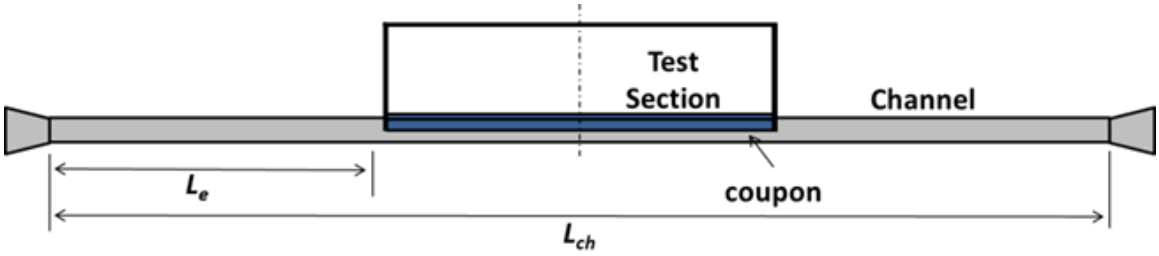

Figure 16: Schematic of coolant supply channel

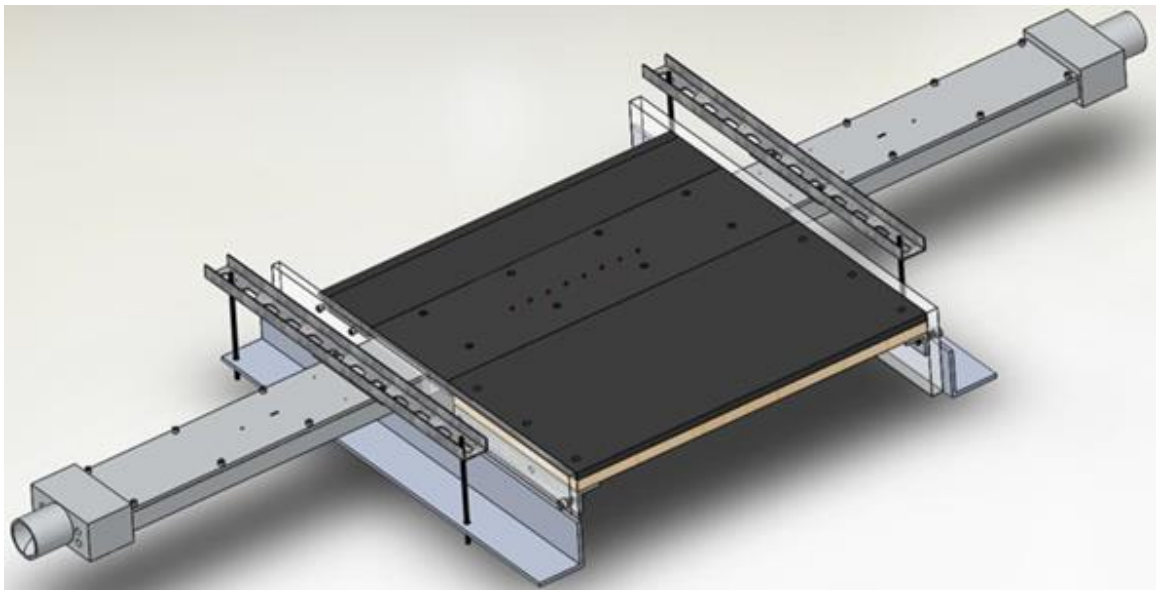

Figure 17: Schematic of 8x coupon and channel assembly

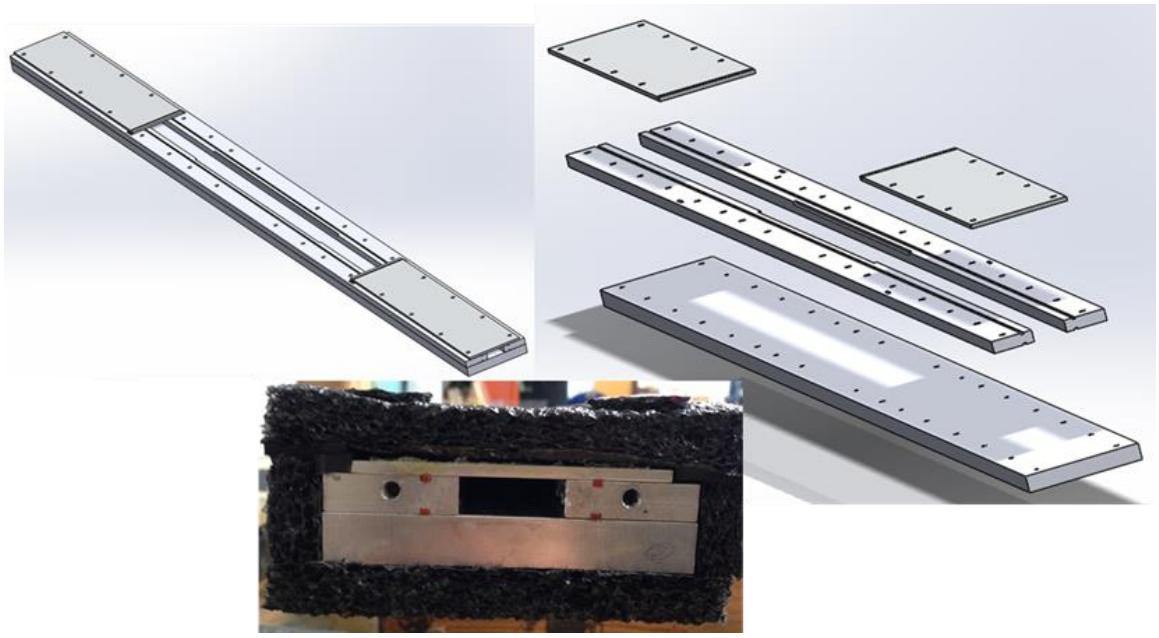

Figure 18: Schematic and assembly of 4x scale modular channel

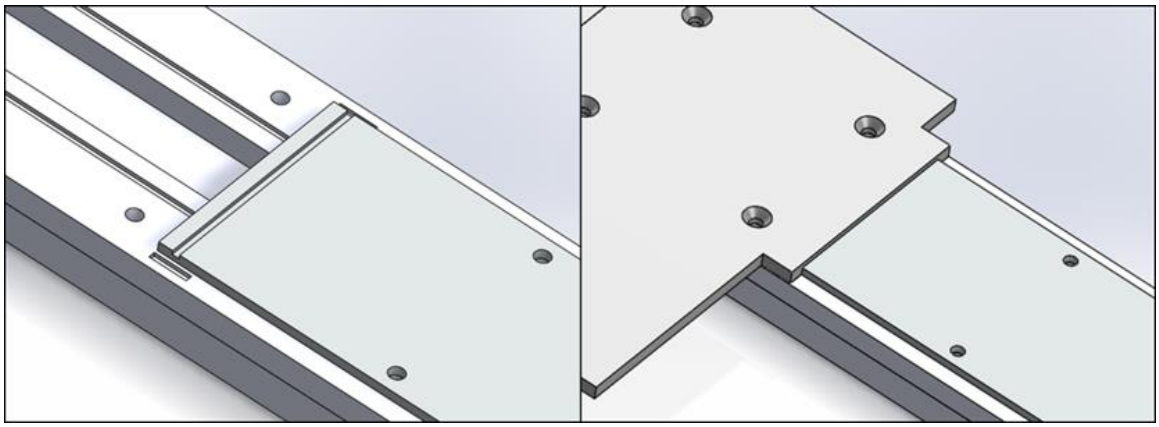

Figure 19: Method of sealing 4x test coupon against crossflow channel

The test coupon and channel were assembled outside of the tunnel and secured using 10-32 bolts. The bolts fastening the coupon to the channel were countersunk to be flush with the coupon surface. Spackle was applied over these bolts and then sanded down to ensure a smooth surface across the entire test coupon surface. The coupon/channel assembly was then carefully slid into the test section through portals on the side of the wind tunnel. The coupon/channel assembly was adjusted once in the test section to be flat and level with the downstream lip of the leading edge. Spackle was applied and sanded down to ensure that the seam between the leading edge and test coupon was as smooth as possible.

The flow through the crossflow channel was specified to be fully developed flow at the inlet to the cooling hole. A velocity profile at the lateral center of the 8x scale channel and upstream location of the cooling hole inlets was measured using a Preston tube, shown in Figure 20. There is no universal, easily comparable correlation to determine whether or not the approach profile was fully developed. To establish whether the channel was fully developed, a second velocity profile was taken at the exit of the

channel with the cooling holes blocked, shown as the Long Development Profile in Figure 20. The two profiles agreed with one another within uncertainty, proving that the flow through the channel was fully developed turbulent flow. The approach profile was also compared with a 1/7 power law profile and had a similar shape, giving a decent indication that the flow was fully developed turbulent. The velocity profile of the 4x scale channel was not measured, but since the inlet flow was the same to both channels and the 4x channel had a longer development length ($L_e = 34.3d_H$) than the 8x channel, the flow through the 4x scale channel was expected to also be fully developed turbulent flow at the cooling hole inlets.

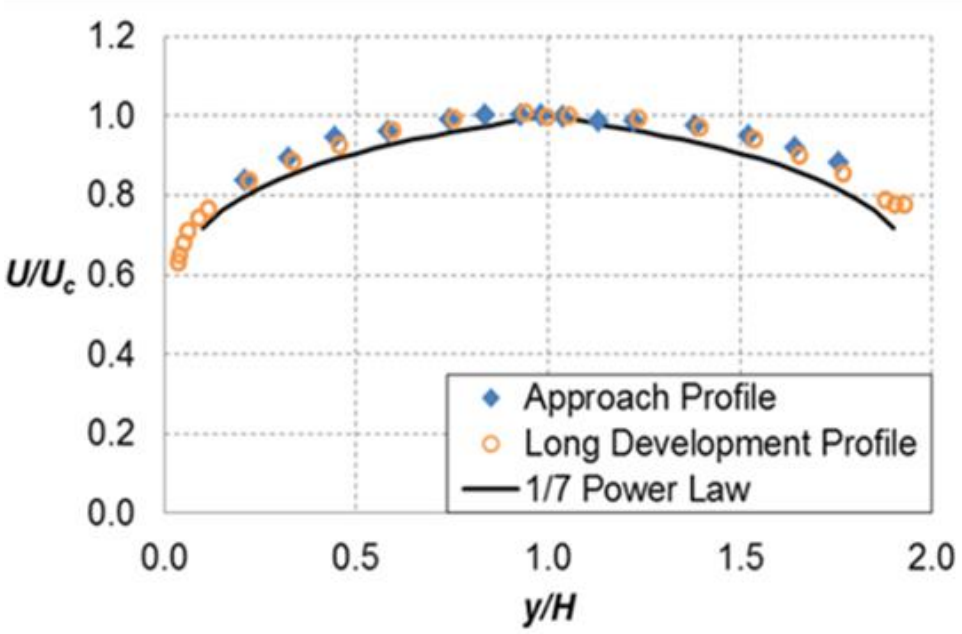

Figure 20: Velocity profile along 8x scale channel centerline

The entrance and exit to the 4x scale channel were connected to the coolant loop by aluminum pipes welded to aluminum plates, as shown in Figure 21. A slot the size of the channel opening was cut through the middle of the aluminum plate. This connector allowed the rectangular channel to be fed by circular coolant piping. The coolant loop is shown connected to the wind tunnel in Figure 22. The wind tunnel facility used for the experiments in this study ran at mainstream temperatures close to room temperature. To match coolant to mainstream density ratios of actual engine conditions where the mainstream is run at much higher temperatures, liquid nitrogen was used to produce a coolant much colder than ambient conditions. Liquid nitrogen was supplied to the coolant piping by a dewar where it entered a shell/tube coolant heat exchanger. Depending on the experiment, either the nitrogen entering the heat exchanger cooled air pulled from the main flow loop which was used as coolant or the nitrogen was warmed by air from the main flow loop and the nitrogen was used as coolant. This will be discussed further in the Testing of the 4x Scale Model section. The temperature of the coolant exiting the heat exchanger could be adjusted to obtain the appropriate density ratio by increasing or decreasing the amount of liquid nitrogen or main tunnel air being supplied. The nitrogen gas or air not used as coolant leaving the heat exchanger was dumped into the main flow loop while the coolant was pumped through the coolant system by an adjustable 7.5 kW coolant blower. The coolant flowed through an orifice meter at the inlet to the crossflow channel to measure the flow rate of coolant into the channel. The coolant leaving the channel flowed through an exit flow meter that measured the flow rate of coolant leaving the channel. For the 8x scale experiments, a Venturi meter was used as the exit flow meter, but for the 4x scale experiments an orifice meter with a smaller diameter was used to obtain more accurate flow measurements at the lower flow rates. The inlet orifice

meter was calibrated according to ASME standard and the exit flow meter was calibrated against the inlet orifice meter with the coolant holes blocked to remove any bias errors between the two flow measurements. The flow rate of coolant through the film cooling holes was calculated as the difference between the flow rate into and out of the channel. The coolant that did not flow through the film cooling holes exited the channel and was exhausted back into the main flow loop. Both the channel and the coolant loop were substantially insulated to minimize heating of the coolant by the ambient as it flowed to and through the crossflow channel.

Figure 21: 4x scale channel to coolant piping connector

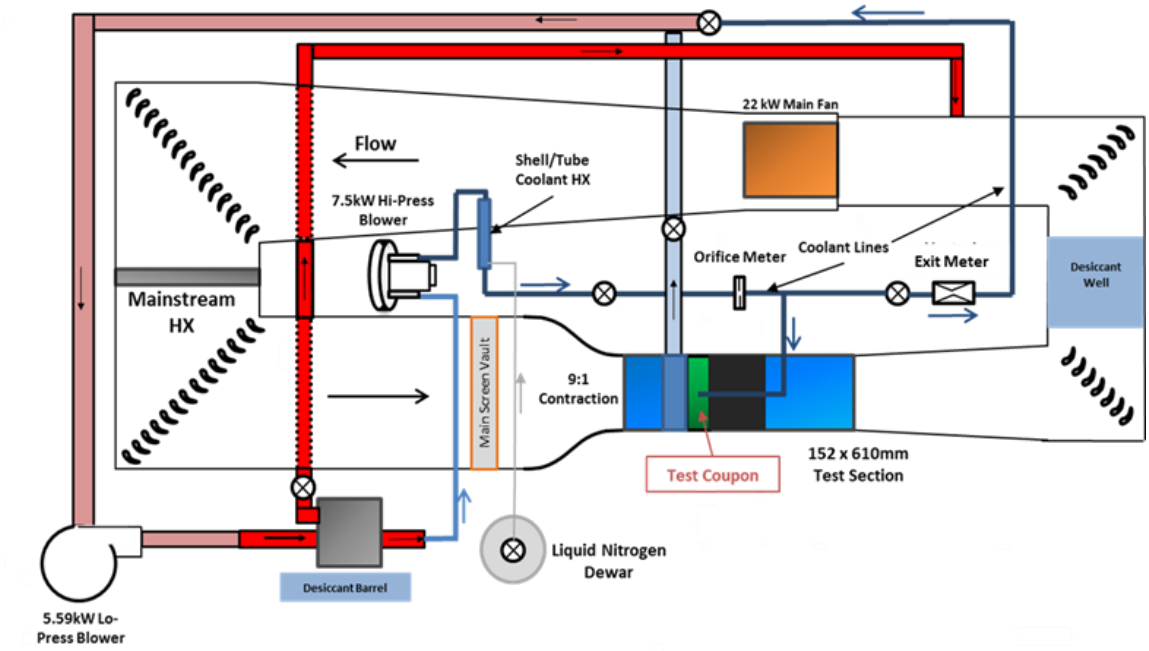

Figure 22: Schematic of wind tunnel and coolant flow loop

The main flow loop was kept at a constant T_∞ = 310 K within 1 K by a mainstream heat exchanger, located as shown in Figure 22. To maintain mainstream temperatures for a wide range of mainstream velocities, both a heater and a chiller were connected to the wind tunnel system. Water from the heater and chiller were mixed before entering the mainstream heat exchanger. After the heat exchanger, the mainstream flow was pushed through the Main Screen Vault, as shown in Figure 22, made up of a honeycomb and fine screens to reduce the free stream turbulence of the flow before entering the nozzle and test section. A Desiccant Well was installed in the main flow loop of the wind tunnel and a Desiccant Barrel in the suction loop of the wind tunnel. The Desiccant Well and Barrel each contained three 18" wide, 32" long, 1 ¼" thick desiccant packs filled with molecular sieve desiccant, type 13X, to remove moisture from the

tunnel air. The coolant used in these experiments reached temperatures close to T_c = 200 K, which was lower than the freezing point of water. Consequently, if the tunnel air was not sufficiently dried prior to and during experimentation, frost would form in and around the cooling holes, disrupting the cooling hole jets. The humidity of the tunnel air was monitored during experiments and remained below 1.0 % for all conditions.

TEMPERATURE MEASUREMENTS

The mainstream and coolant temperatures were measured with Type E thermocouples. The mainstream thermocouples were calibrated against a glycol water bath. Three thermocouples were extended into the mainstream flow upstream of the turbulence grid. The average of these three thermocouples was used as the calculated mainstream temperature. The calibration curve for the center mainstream thermocouple is shown in Figure 23. By self-calibrating the thermocouples instead of using the NIST Standard calibration, the uncertainty in mainstream temperature was decreased from ± 1 K to ± 0.5 K. The coolant thermocouples, however, were calibrated using the NIST Standard and therefore had an uncertainty in T_c of ± 1 K. Coolant temperatures were measured at the inlet and outlet of the crossflow channel. The temperature of the coolant exiting the film cooling holes was calculated as the average between these two temperatures. This method of calculating hole coolant temperature has agreed with measurements of the temperature exiting the hole within ± 1 K in past experiments.

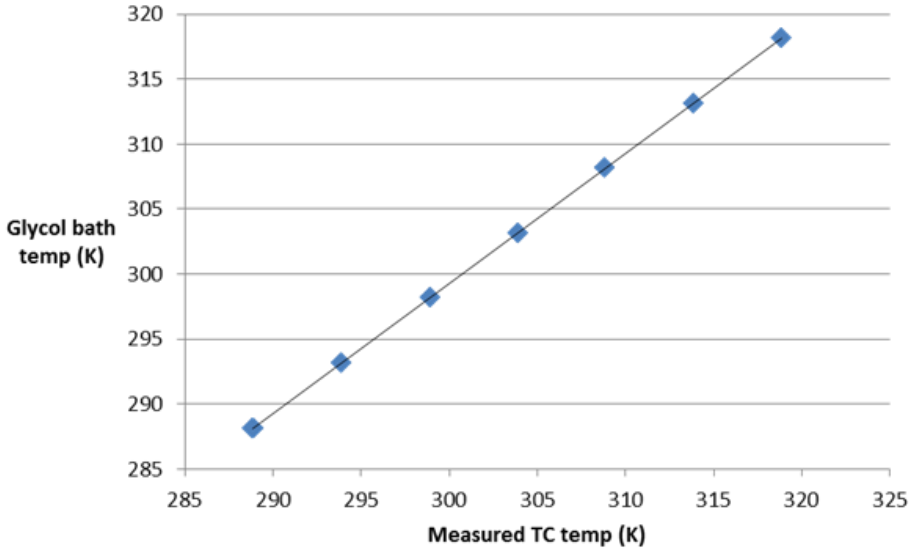

Figure 23: Example of mainstream thermocouple calibration curve

Temperature measurements of the test coupon surface used to calculate adiabatic effectiveness were made using infrared (IR) thermography. A forward-looking, Flir model A655, IR camera was used to view the entire downstream area from $x/d = 0 – 55$ for all conditions. IR cameras cannot image through the acrylic walls of the test section, so a 150 mm by 100 mm Zinc Selenide (ZnSe) window was installed in the top of the test section, shown in Figure 24. A camera mount was constructed as shown in Figure 25 to easily adjust the position and angle of the camera to accommodate the different testing conditions. Coverings were taped around the IR camera to prevent glare off of the ZnSe window. The surfaces of the coupon and test section were painted black with ultra-flat spray paint to guarantee a uniform surface emissivity. In-situ IR calibrations were performed prior to experimentation by mounting thin ribbon surface E-type thermocouples onto copper plates, also spray painted black, and securing them at the exit

of the cooling holes. During tunnel cool-down, a succession of images was taken of the test section surface. As the temperature of the coolant jets decreased, a calibration between the actual temperature of the surface measured by the thermocouples and the temperature of the surface measured by the IR camera was obtained for a range of temperatures. The IR calibration for the A655 camera with the 25 degree lens used for imaging the 4x scale cooling holes is shown in Figure 26 with a second order polynomial calibration curve. The IR camera calibration resulted in a bias uncertainty in T_w of ± 0.4 K determined by propagating each surface thermocouple measurement by the standard error of fit of the calibration curve and calculating the propagated curve fit coefficients. From this method, an uncertainty in the wall temperature due to the calibration was estimated.

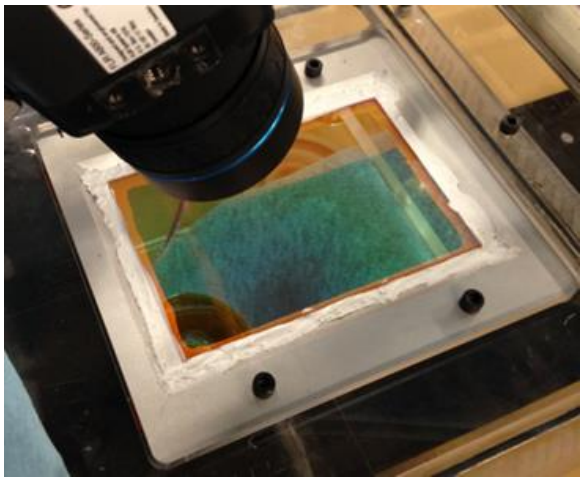

Figure 24: ZnSe window above wind tunnel test section

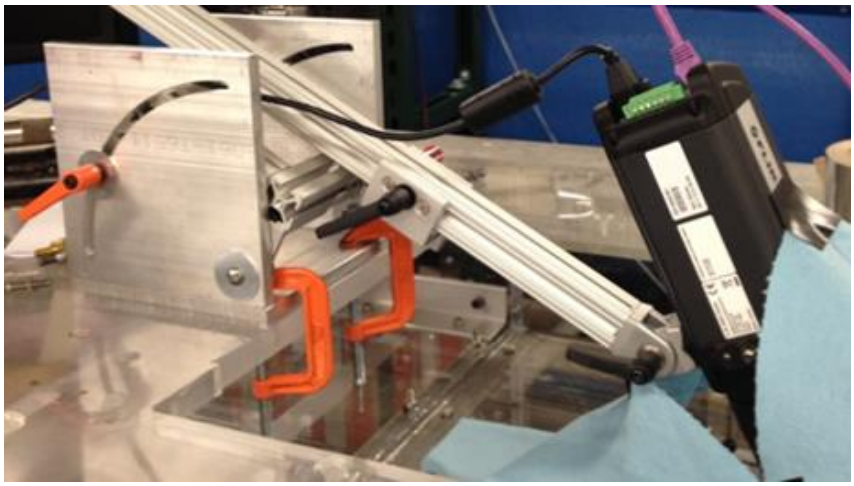

Figure 25: Adjustable IR camera mount

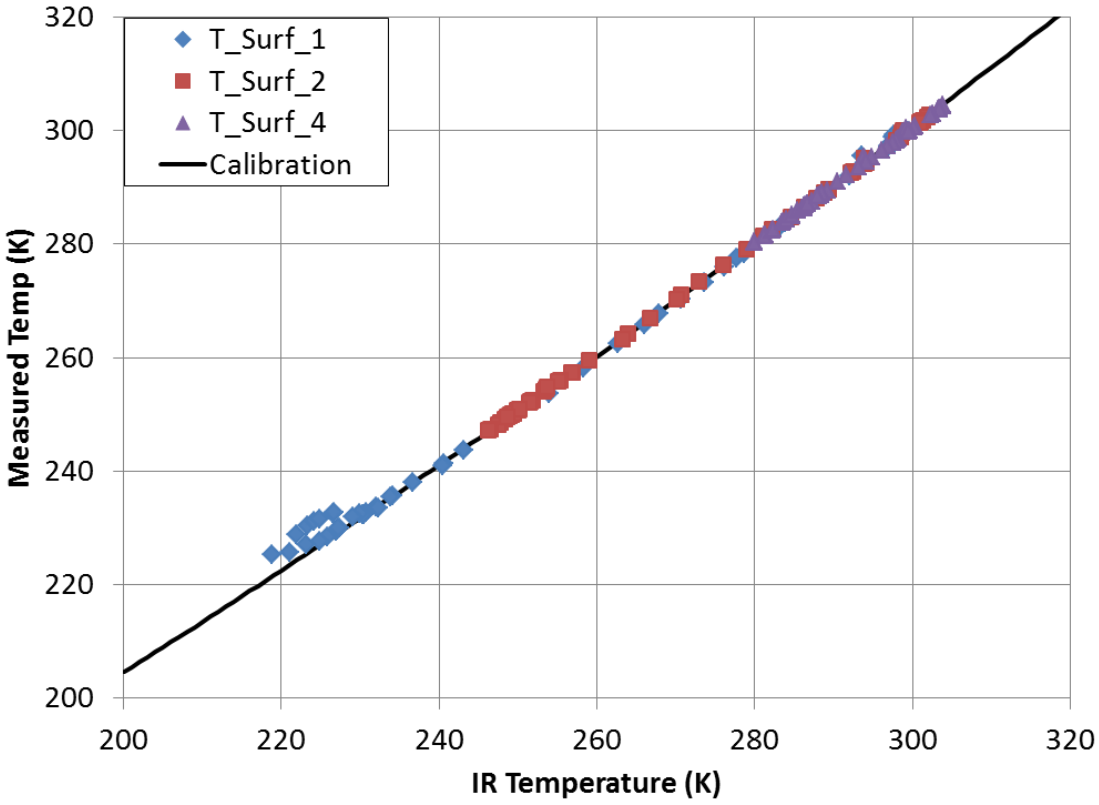

Figure 26: A655 IR camera 25 degree lens second order calibration curve

DESIGN OF OPERATIONAL PARAMETERS

The key operational parameters of this study were mainstream Mach number Ma_∞, mainstream Reynolds number based on cooling hole diameter $Re_{\infty,d}$, coolant to mainstream density ratio DR, blowing ratio M, coolant velocity ratio VR, Reynolds number at the crossflow channel inlet Re_{ch}, and channel velocity ratio VR_{ch}. These parameters were calculated from equations 6 - 12. For each condition, adiabatic effectiveness measurements were taken at cooling velocity ratios of VR = 0.5, 1.1, and 1.7. For each coolant velocity ratio, five IR images were taken over a five to ten minute interval to ensure that the surface temperature of the flat plate had reached steady state. At each coolant velocity ratio for a certain condition, all operational parameters were held constant throughout imaging. The mainstream velocity was steady within ± 1 m/s, the density ratio within ± 0.01, the coolant velocity ratio within ± 0.05, and the channel Reynolds number within ± 1,000.

$$Ma_\infty = \frac{U_\infty}{\sqrt{\gamma R T_\infty}} \tag{6}$$

$$Re_{\infty,d} = \frac{\rho_\infty U_\infty d_H}{\mu_\infty} \tag{7}$$

$$DR = \frac{\rho_c}{\rho_\infty} \tag{8}$$

$$M = \frac{\rho_c U_c}{\rho_\infty U_\infty} \tag{9}$$

$$VR = \frac{M}{DR} = \frac{U_c}{U_\infty} \tag{10}$$

$$Re_{ch} = \frac{\rho_c d_H U_{ch}}{\mu_c} \tag{11}$$

$$VR_{ch} = \frac{U_{ch}}{U_\infty} \tag{12}$$

The purpose of this study was to examine the effects of channel Reynolds number and channel velocity ratio on the adiabatic effectiveness of shaped hole film cooling. Tests 2 and 3, shown in Table 1, were compared to show the effect of channel Reynolds number and Tests 2 and 4 were compared to show the effect of channel velocity ratio. Ideally all parameters would be the same between these comparisons except the parameter specifically being investigated. However, because two scaled models were used, matching all operational parameters except channel velocity ratio or Reynolds number resulted in no variability in either parameter. In order to vary channel Reynolds number and channel velocity ratio independently, other parameters had to be allowed to vary. Initially it was presumed that the mainstream Reynolds number had only a weak effect of film cooling performance and would be varied to obtain a large range of channel velocity ratios and channel Reynolds numbers. However, results from a study being completed concurrently by Anderson et al. [18], showed that this range of mainstream Reynolds numbers for the same shaped hole actually had a substantial effect on film cooling effectiveness. This same study also showed that if maintaining a constant δ^*/d, mainstream Mach numbers between Ma_∞ = 0.08 – 0.15 had little to no effect on film cooling performance. Knowing that density ratio had a weak effect on film cooling performance, the parameters in Table 1 were chosen, tolerating slight differences in density ratio (and mainstream Mach number, but this was found to have minimal

influence on effectiveness) between comparisons to investigate the channel Reynolds number and channel velocity ratio independently of each other.

DENSITY RATIO CORRECTION

A study by Anderson et al. [19] found that laterally averaged adiabatic effectiveness at different density ratios scaled most appropriately with coolant velocity ratio, as shown in Figure 27. The density ratio curves had different laterally averaged effectiveness, but their peaks and trends collapsed well when scaled with coolant velocity ratio. However, the data from [19] only contained data up to *DR* = 1.5. Another Anderson et al. study [18] contained adiabatic effectiveness data at *DR* = 1.8 for the same 7-7-7 hole geometry under nominally the same experimental conditions. Using the data from both studies, a density ratio correction factor was calculated from equation 13 that could be applied to the 4x scale data at *DR* = 1.5 to compare it to the 8x scale data at *DR* = 1.8.

$$CF = \frac{\eta_{DR=1.5}}{\eta_{DR=1.8}} \tag{13}$$

Laterally averaged values interpolated from the data from both studies to obtain the comparable coolant velocity ratios are plotted as a function of density ratio in Figure 28 for the three coolant velocity ratios. The trend was generally an increase in adiabatic effectiveness with increasing density ratio, resulting in correction factors above one, except at the farthest downstream positions where the effectiveness decreases slightly for *VR* = 0.5 and 1.7. Correction factors were calculated at each *x/d* position for all three velocity ratios, shown in Figure 29. A second order polynomial was fit to this series of correction factors as a function of downstream position for each coolant velocity ratio.

Anderson et al. [18] only presented data up to $x/d = 25$, so downstream of this position a linear trend was devised to predict the correction factor. The trend was created with the assumption that far enough downstream the effectiveness would approach zero and the density ratio correction factor would approach unity. After $x/d = 25$, the correction factor trend was a linear line approaching $CF = 1$ by $x/d = 100$.

The effect of the density ratio correction on laterally averaged adiabatic effectiveness is shown in Figure 30. There was little difference between the corrected and uncorrected data downstream of $x/d = 25$ at any coolant velocity ratio. Upstream of $x/d = 25$ for the $VR = 0.5$ and 1.7 cases, the density ratio correction increased the effectiveness by less than $\bar{\eta} = 0.01$. The density ratio correction had a larger effect at $VR = 1.1$ where the correction increased the effectiveness by $\bar{\eta} = 0.02$.

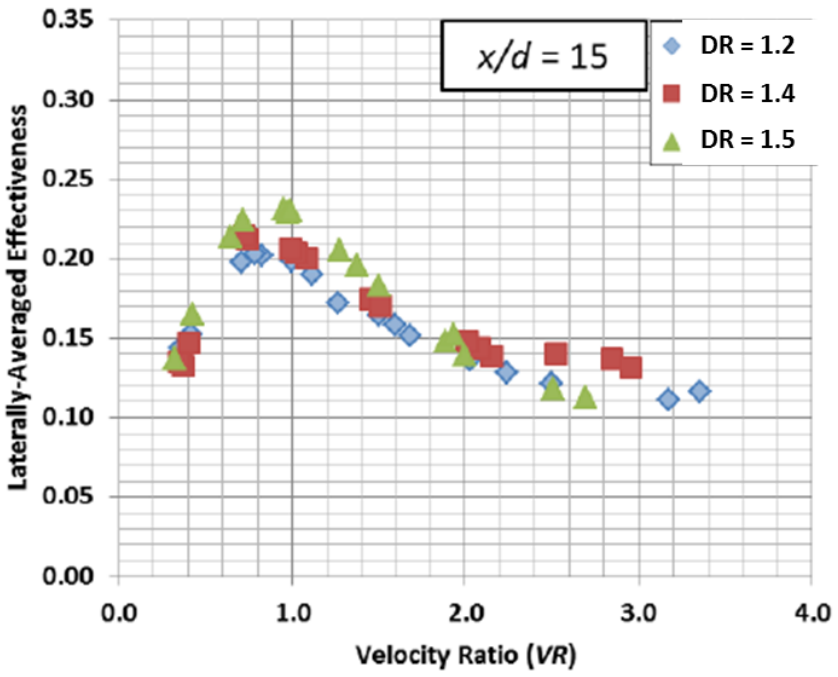

Figure 27: Laterally averaged effectiveness of shaped holes as a function of coolant velocity ratio [19]

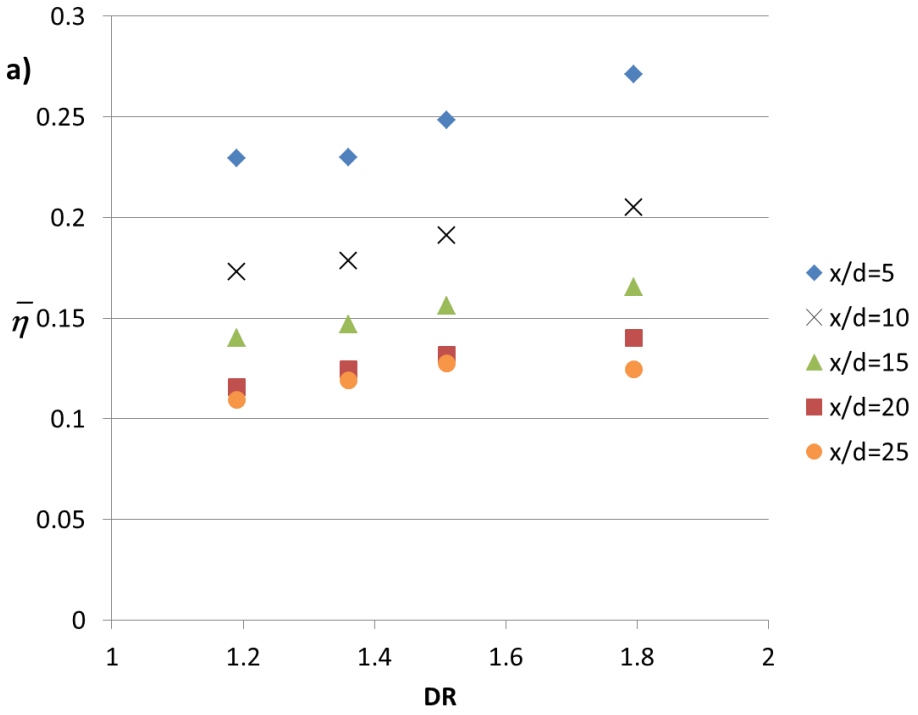
a)
0.3
0.25
0.2
0.15
0.1
0.05
0
$\bar{\eta}$
1
1.2
1.4
1.6
1.8
2
DR
x/d=5
x/d=10
x/d=15
x/d=20
x/d=25

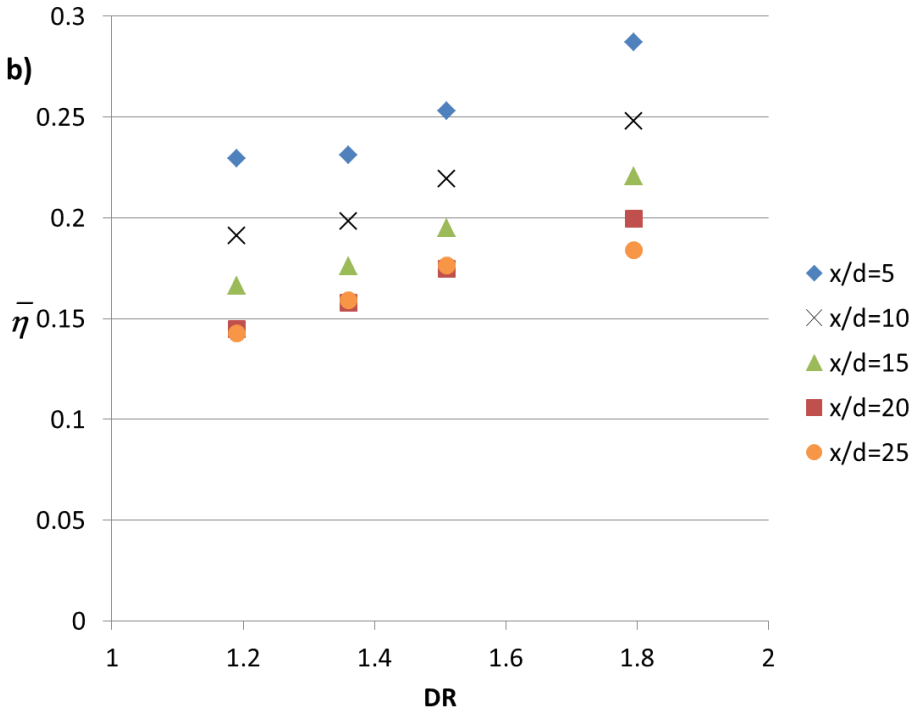
b)
0.3
0.25
0.2
0.15
0.1
0.05
0
$\bar{\eta}$
1
1.2
1.4
1.6
1.8
2
DR
x/d=5
x/d=10
x/d=15
x/d=20
x/d=25

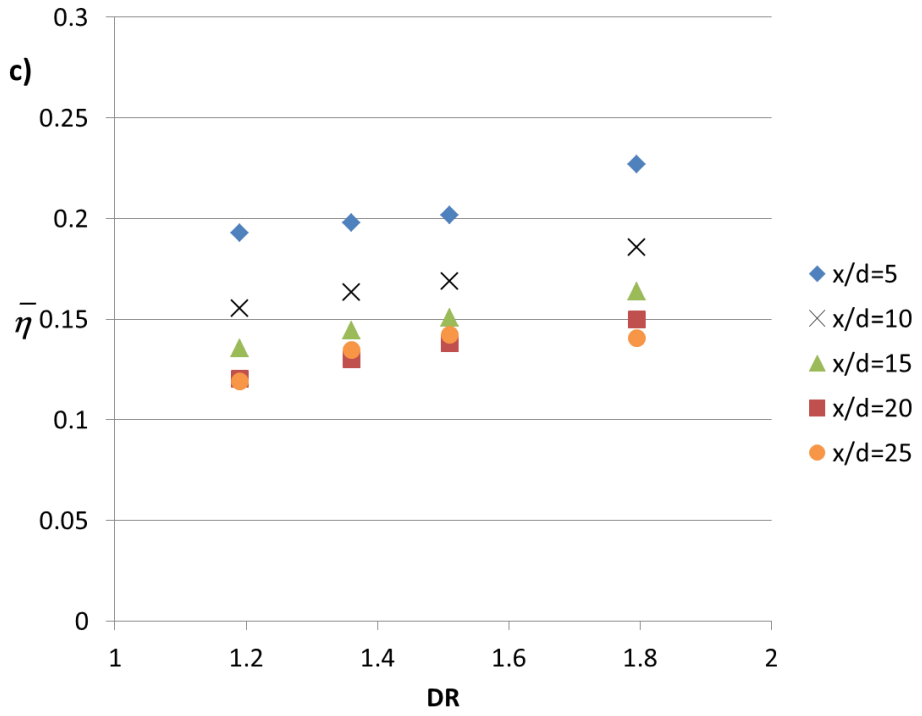

Figure 28: Laterally averaged adiabatic effectiveness values as a function of density ratio for various x/d positions obtained from [19] and [18] at a) VR = 0.5, b) VR = 1.1, and c) VR = 1.7

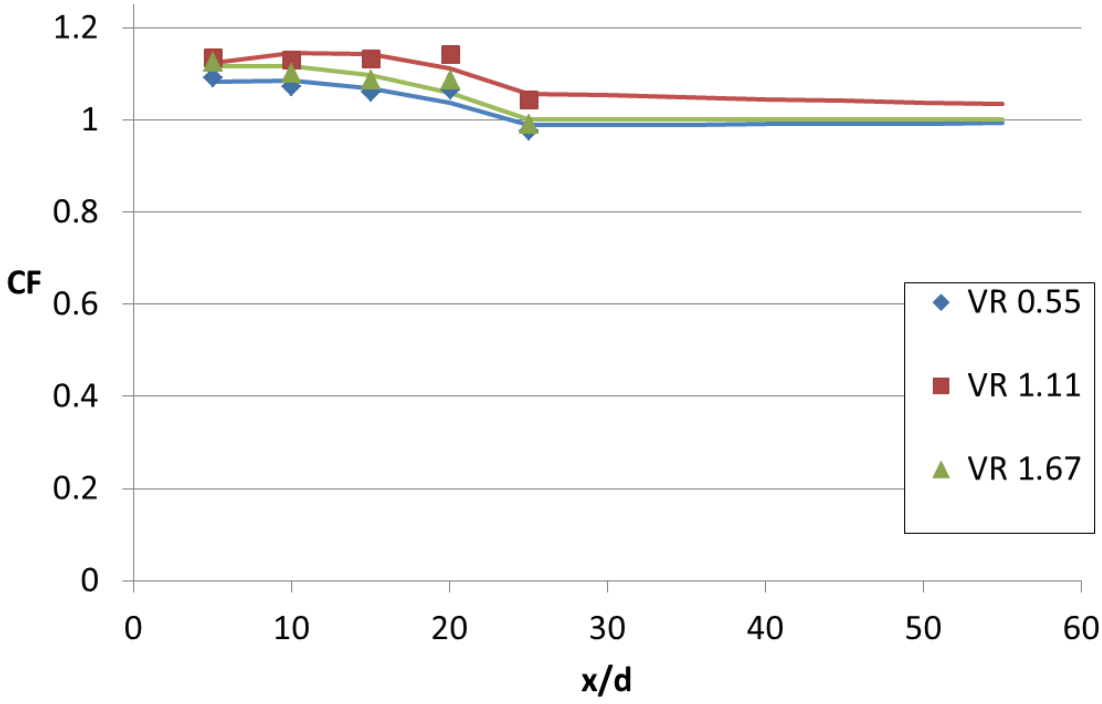

Figure 29: Plot of DR correction factor as a function of downstream position for all coolant velocity ratios

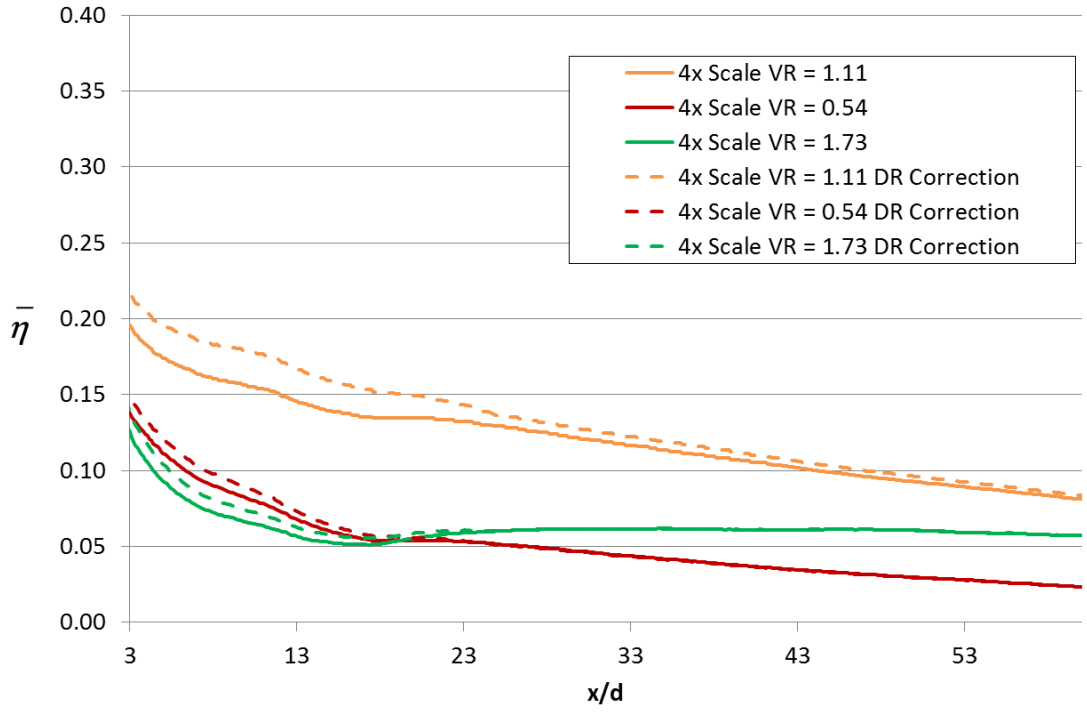

Figure 30: Effect of density ratio correction on the laterally averaged adiabatic effectiveness of the 4x scale results at Re_{ch} = 57,000

TESTING OF THE 4X SCALE MODEL

The 8x scale model had been used in previous studies and therefore had a smooth and refined testing process. This study was the first to test the 4x scale film cooling model. Installing the 4x scale with the cooling loop used for the 8x scale model led to poor results. The coolant loop was designed to run coolant flow rates for 8x scale experiments of $\dot{m}$ = 22 – 31 g/s. To obtain the conditions specified for the 4x scale experiments, the coolant loop was experiencing flow rates of $\dot{m}$ = 2 – 14 g/s, an order of magnitude less than for the 8x scale experiments. Some desired conditions could not be met due to inefficiencies in the large coolant heat exchanger at the different conditions

and the inability of the flow meters to accurately measure the low flow rates caused uncertainties in coolant velocity ratio approaching 30 %. To successfully test the 4x scale model, the flow was rerouted to a smaller heat exchanger, the inlet orifice meter and exit Venturi meter were replaced by smaller diameter orifice meters, and the flow pressure readings were switched to pressure transducers with smaller pressure ranges. The 4x scale experiments still resulted in higher uncertainties than the 8x scale experiments, but these uncertainties, discussed later, were acceptable.

A second difficulty in testing the 4x scale model was the presence of frost build-up in and around the cooling holes. The 8x scale conditions were operated using air as coolant where the liquid nitrogen from the dewar was used to cool air pulled from the tunnel mainstream to the appropriate density ratio. Even though the tunnel humidity levels were always below 1 % (generally around 0.5 %), a light dusting of frost still formed in and at the exit of the cooling holes. The light dusting of frost had negligible effect of the performance of the 8x scale model; however it had significant effects on the performance of the 4x scale model when operated with air as coolant. Frost formation caused variability in the performance of the cooling holes and the uncertainty associated with that variation was difficult to determine. For each operating condition, several images were taken to ensure repeatability and that the tunnel was at steady state. Lateral effectiveness profiles for multiple images of the same condition for the 4x scale model at VR = 0.5 are shown in Figure 31. For comparison, lateral effectiveness profiles for multiple images for the 8x scale model at VR = 0.5 are shown in Figure 32. The image-to-image and hole-to-hole variability was minimal for the 8x scale model, varying at the most by 3 %. The image-to-image and hole-to-hole variability for the 4x scale model was substantial, fluctuating at the worst from effectiveness values of η = 0.46 – 0.24. The

image to image variation was due to transient effects in the tunnel, mostly attributed to frost formation. The hole-to-hole variation though, was partly due to small inconsistencies in hole-to-hole machining causing differences in the hole dimensions. To resolve whether or not the hole to hole variation in effectiveness was due to the slight differences in hole geometry, Figure 33 presents the same laterally averaged profiles as in Figure 31, but compared with a laterally averaged profile of the holes at a different condition, but when frost was not present. The 'no frost' profile exhibited a fair amount of hole to hole variation, particularly outside of the center four film cooling holes. However, holes that had the lowest effectiveness without frost were not consistently the lowest performers when frost was present and the same for holes that had high effectiveness without frost. The hole-to-hole variation could not, then, be attributed solely to machining differences and the presence of frost ultimately resulted in uncertainties in adiabatic effectiveness so large that no conclusions could be confidently made. To reduce frost buildup in and around the coolant holes, the coolant loop was switched to run nitrogen as coolant where liquid nitrogen from the dewar was warmed by air pulled from the tunnel mainstream to the appropriate density ratio. Operating the tunnel in this fashion successfully reduced hole-to-hole and image-to-image variation as shown in Figure 34, but required a longer period of time to reach steady state conditions. As can be seen in Figure 34, the tunnel conditions were not at steady state when images 43 – 48 were taken, but the lateral profiles of those images approached the steady state performance recorded by images 49 and 50.

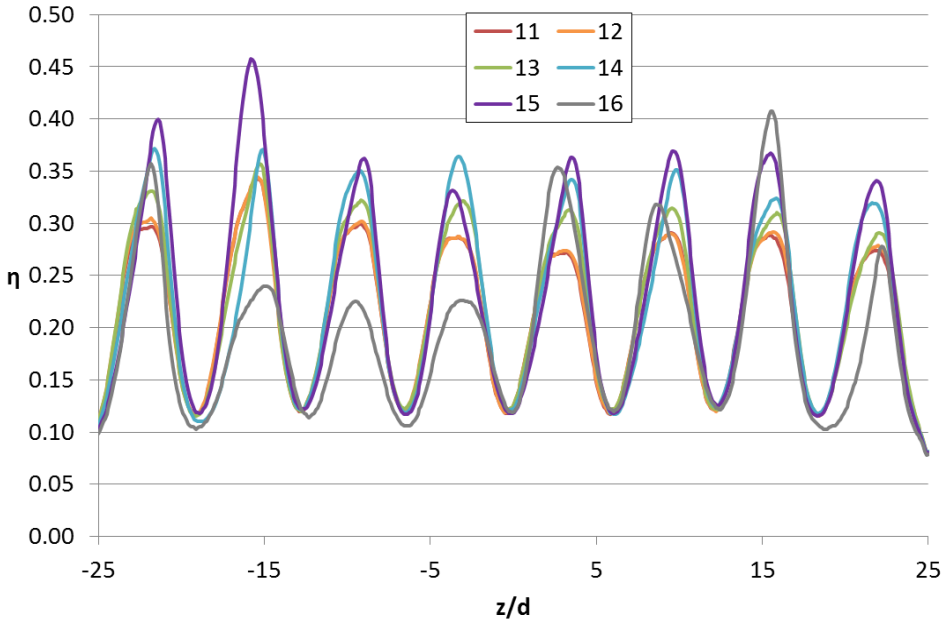

Figure 31: Example of poor uniformity from initial experiments for the 4x scale holes at VR = 0.5, Re_{ch} = 57,000 and x/d = 10

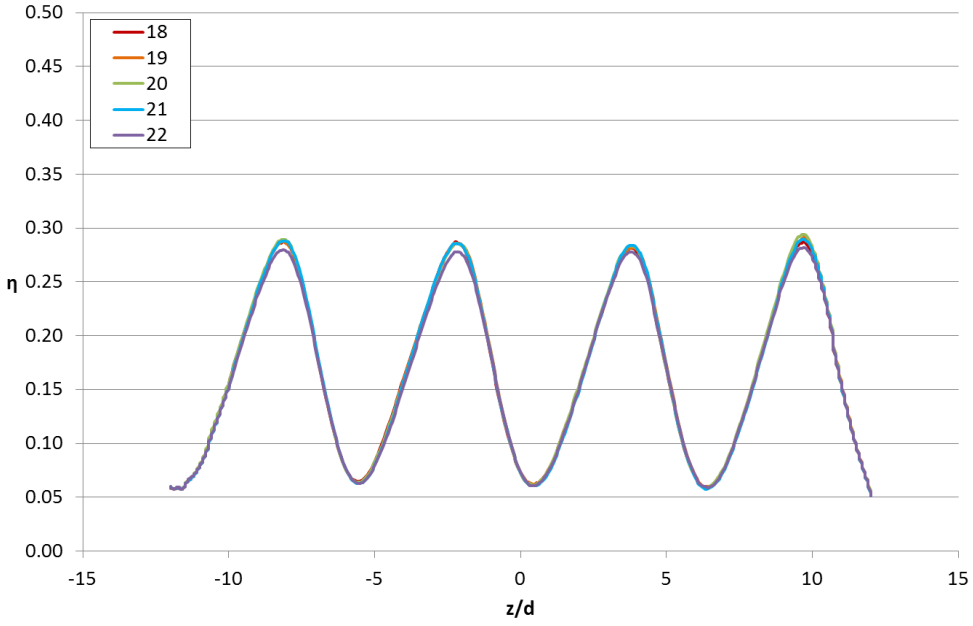

Figure 32: Lateral profiles of adiabatic effectiveness for a succession of images for the 8x scale holes at VR = 0.5 and x/d = 10

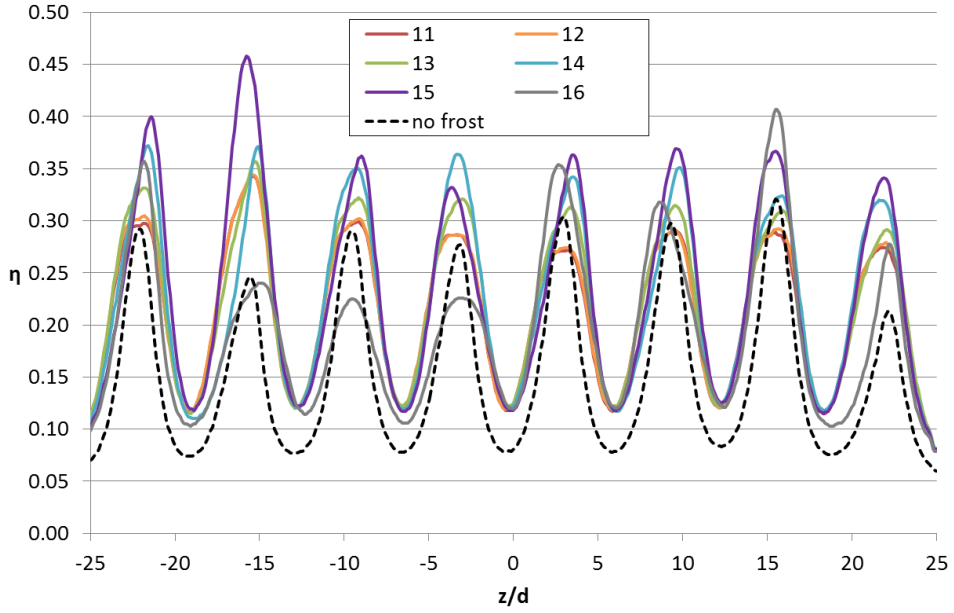

Figure 33: Lateral profiles of adiabatic effectiveness for the 4x scale holes compared to a profile not influenced by frost

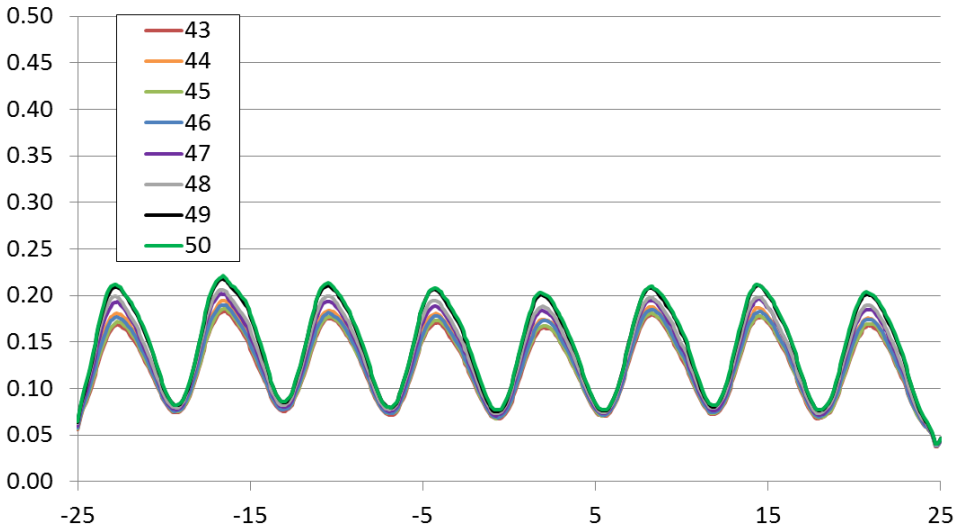

Figure 34: Lateral profiles of adiabatic effectiveness for a succession of images for 4x scale holes at VR = 0.5, Re_{ch} = 57,000 and x/d = 10 using nitrogen as coolant

CONDUCTION CORRECTION

As was already mentioned, the surface of the test section was desired to be as adiabatic as possible to accurately calculate adiabatic effectiveness. Even though polyurethane foam had a low thermal conductivity, there was still heat transfer through the test section floor. A finite element conduction correction technique described in [20] and [21] was used to remove these conduction errors. A different conduction model was used for the 8x scale model and the 4x scale model to account for the differences in coupon material and operational parameters. A comparison of uncorrected and COMSOL conduction corrected adiabatic effectiveness contours for the 8x and 4x scale models at a coolant velocity ratio of $VR = 1.1$ is shown in Figures 35 and 36 respectively. Comparing the uncorrected and corrected contours for the 8x scale model, the conduction correction removed the through wall conduction that caused deceptively high effectiveness between the coolant jets in the uncorrected contour. For the 4x scale model, there was a much greater difference between the uncorrected and corrected contours due to the high thermal conductivity of the CPVC material. The conduction correction was able to remove the through wall conduction errors everywhere except upstream of about $x/d = 3$. This position was the location of the seam between the CPVC coupon and the polyurethane foam sheet on the test coupon. The COMSOL model was unable to account for the appropriate conduction through the upstream CPVC. The COMSOL model began at $x/d = 0.6$ and did not include the cooling holes themselves. An adiabatic boundary condition was used at the upstream edge of the CPVC, so any conduction through the CPVC due to the cooling holes was neglected. Due to the falsely high effectiveness upstream of $x/d = 3$ for the 4x scale model results, all conclusions from laterally averaged data was based on data downstream of $x/d = 3$.

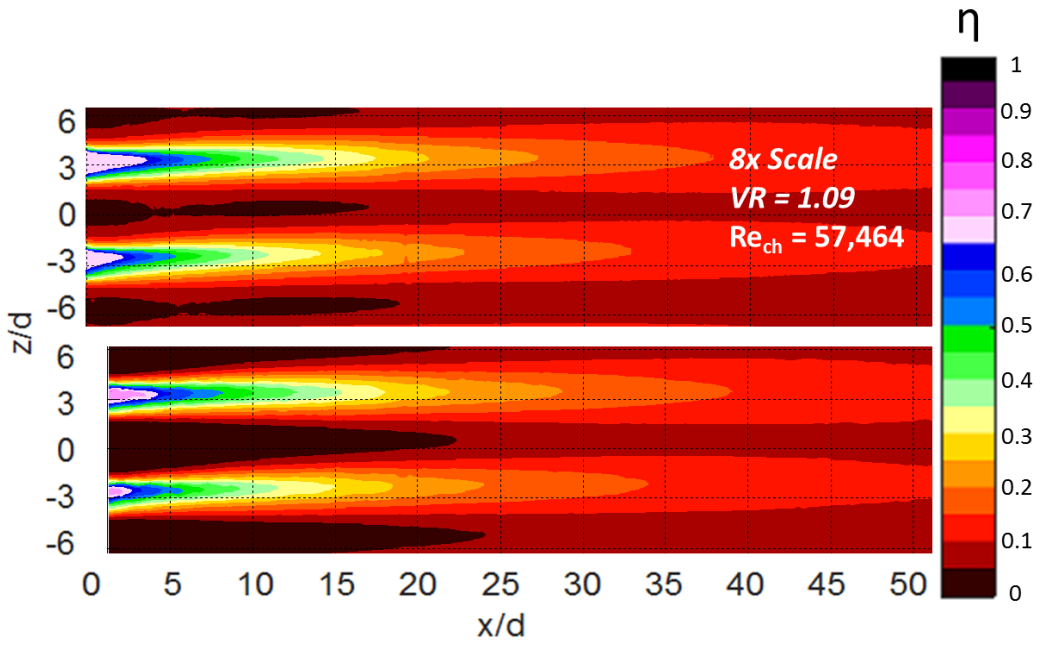

Figure 35: Adiabatic effectiveness contours for the 8x scale model at VR = 1.1 and Re_{ch} = 57,000 Top: uncorrected for conduction Bottom: corrected for conduction

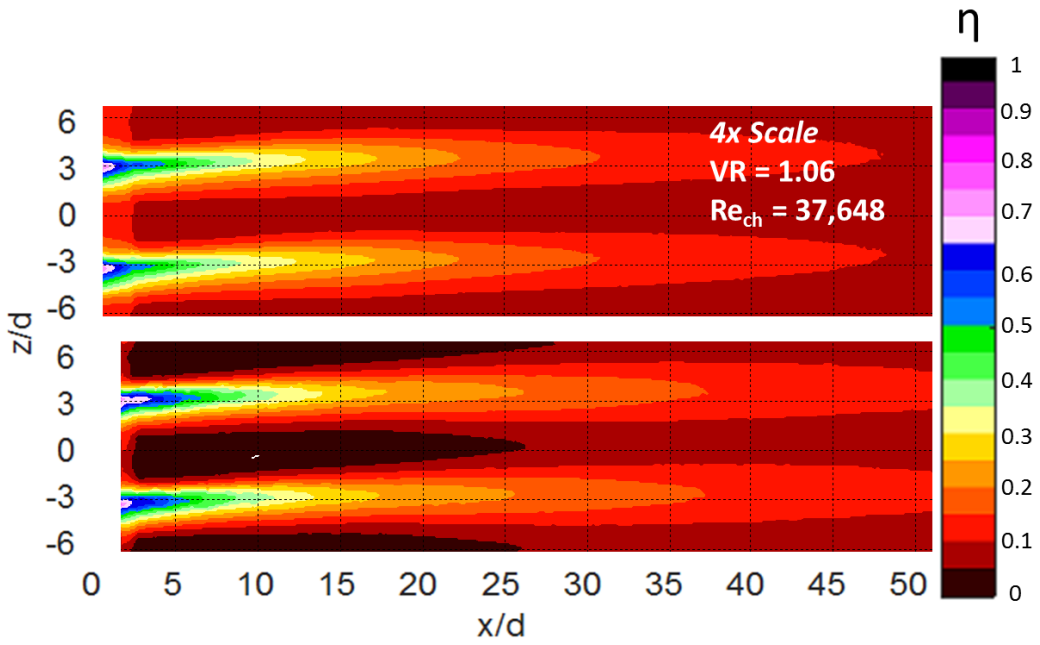

Figure 36: Adiabatic effectiveness contours for the 4x scale model at VR = 1.1 and Re_{ch} = 38,000 Top: uncorrected for conduction Bottom: corrected for conduction

UNCERTAINTY ANALYSIS AND REPEATABILITY

The uncertainties in the presented values of operational parameters and adiabatic effectiveness were calculated by sequentially perturbing bias and precision uncertainties associated with the raw data measurements. Temperature, pressure, and dimensional measurements were the only measurements used to calculate operational parameters. Each raw measurement was perturbed by its uncertainty and used to calculate the operational parameter of interest. The difference between this perturbed operational parameter and the nominal operational parameter was the uncertainty in the operational parameter due to the uncertainty in the raw measurement. The root-sum-square of these differences was calculated to determine a total uncertainty in the operational parameter. Summary charts of the bias and precision uncertainties in operational parameters for all experimental conditions tested are shown in Tables 3, 4, and 5. Due to the high number of 500 samples for each measurement, the precision uncertainty in the operational parameters was negligible. The uncertainty in operational parameters was dominated by bias uncertainty. On the whole, the 8x scale conditions had slightly lower bias uncertainties than the 4x scale conditions. Bias and precision uncertainties for all operational parameters except coolant velocity ratio were below 3%. However, the uncertainties in coolant velocity ratio ranged from 3 % to 13 %. The largest uncertainties in coolant velocity ratio were consistently at the lowest coolant velocity ratio of $VR = 0.5$. Tables 6, 7, and 8 show the bias and precision uncertainty contributions of the raw measurements to the uncertainty in coolant velocity ratio for the three conditions at $VR = 0.5$. The third and fifth column of every table presents the contributing uncertainty to velocity ratio of the measured parameter. The total uncertainty in coolant velocity ratio is a root-sum-squared of these contributing uncertainties. Majority of the bias uncertainty in

coolant velocity ratio was due to the uncertainty in hole diameter and static pressure and pressure differential measurements across the flow meters.

Perturbing the uncertainty in the measured mainstream, coolant, and wall temperatures resulted in a precision uncertainty in adiabatic effectiveness of $\delta\eta_p = 0.002$ and a bias uncertainty of $\delta\eta_b = 0.006$. The largest contributor to bias uncertainty in effectiveness was the bias uncertainty in the measured mainstream temperature of $\delta T_\infty = 0.5$ K from the thermocouple calibration. Both the bias uncertainty in the measured wall temperature due to the IR calibration of $\delta T_w = 0.4$ K and the bias uncertainty in the measured coolant temperature specified for the NIST thermocouple calibration of $\delta T_c = 1$ K contributed slightly less to the adiabatic effectiveness bias uncertainty than measured mainstream temperature. These uncertainties were calculated for local adiabatic effectiveness, but the uncertainty in the laterally averaged adiabatic effectiveness was the same.

Table 3: Bias and precision uncertainties of operational parameters for Test 2 (the 8x scale condition)

8x VR=0.55

	x	δx_b	δx_b%	δx_p	δx_p%
Ma_∞	0.069	0.000	1%	0.000	0%
$Re_{\infty,d}$	5,968	139	2%	0	0%
VR_{ch}	0.32	0.004	1%	0.000	0%
Re_{ch}	59,276	1,234	2%	3	0%
DR	1.80	0.005	0%	0.000	0%
VR	0.58	0.04	7%	0.00	0%

8x VR=1.11

	x	δx_b	δx_b%	δx_p	δx_p%
Ma_∞	0.069	0.000	1%	0.000	0%
$Re_{\infty,d}$	6,014	140	2%	0	0%
VR_{ch}	0.32	0.004	1%	0.000	0%
Re_{ch}	58,967	1,227	2%	3	0%
DR	1.80	0.005	0%	0.000	0%
VR	1.14	0.05	4%	0.00	0%

8x VR=1.7

	x	δx_b	δx_b%	δx_p	δx_p%
Ma_∞	0.070	0.000	1%	0.000	0%
$Re_{\infty,d}$	6,072	141	2%	0	0%
VR_{ch}	0.35	0.004	1%	0.000	0%
Re_{ch}	65,286	1,360	2%	4	0%
DR	1.80	0.005	0%	0.000	0%
VR	2.37	0.06	3%	0.00	0%

Table 4: Bias and precision uncertainties of operational parameters for Test 3 (the 4x scale condition at VR_{ch} = 0.36)

4x VRch = 0.36 VR=0.55

	x	δx_b	δx_b%	δx_p	δx_p%
Ma_∞	0.150	0.000	0%	0.000	0%
$Re_{\infty,d}$	5,958	173	3%	0	0%
VR_{ch}	0.43	0.006	1%	0.002	0%
Re_{ch}	35,867	765	2%	2	0%
DR	1.49	0.003	0%	0.000	0%
VR	0.57	0.07	12%	0.00	0%

4x VRch = 0.36 VR=1.11

	x	δx_b	δx_b%	δx_p	δx_p%
Ma_∞	0.150	0.000	0%	0.000	0%
$Re_{\infty,d}$	5,951	173	3%	0	0%
VR_{ch}	0.42	0.006	1%	0.000	0%
Re_{ch}	35,829	765	2%	2	0%
DR	1.52	0.004	0%	0.000	0%
VR	1.09	0.09	8%	0.00	0%

4x VRch = 0.36 VR=1.7

	x	δx_b	δx_b%	δx_p	δx_p%
Ma_∞	0.150	0.000	0%	0.000	0%
$Re_{\infty,d}$	5,959	173	3%	0	0%
VR_{ch}	0.36	0.005	1%	0.000	0%
Re_{ch}	31,364	671	2%	2	0%
DR	1.49	0.003	0%	0.000	0%
VR	1.74	0.13	7%	0.00	0%

Table 5: Bias and precision uncertainties of operational parameters for Test 4 (the 4x scale condition at Re_{ch} = 57,000)

4x Rech = 57,000 VR=0.55

	x	δx_b	δx_b%	δx_p	δx_p%
Ma_∞	0.149	0.000	0%	0.000	0%
$Re_{\infty,d}$	5,941	172	3%	0	0%
VR_{ch}	0.64	0.010	2%	0.000	0%
Re_{ch}	56,610	1,245	2%	2	0%
DR	1.51	0.004	0%	0.000	0%
VR	0.59	0.08	13%	0.00	0%

4x Rech = 57,000 VR=1.11

	x	δx_b	δx_b%	δx_p	δx_p%
Ma_∞	0.150	0.000	0%	0.000	0%
$Re_{\infty,d}$	5,945	172	3%	0	0%
VR_{ch}	0.65	0.011	2%	0.000	0%
Re_{ch}	56,347	1301	2%	2	0%
DR	1.49	0.003	0%	0.000	0%
VR	1.06	0.11	10%	0.00	0%

4x Rech = 57,000 VR=1.7

	x	δx_b	δx_b%	δx_p	δx_p%
Ma_∞	0.150	0.000	0%	0.000	0%
$Re_{\infty,d}$	5,946	172	3%	0	0%
VR_{ch}	0.57	0.009	2%	0.000	0%
Re_{ch}	52,560	1,177	2%	3	0%
DR	1.51	0.004	0%	0.000	0%
VR	1.67	0.10	6%	0.00	0%

Table 6: Bias and precision uncertainty contributions of the raw measurements to the uncertainty in coolant velocity ratio of VR = 0.5 for the 8x scale holes

8x VR=0.5					
	x	δx_b	contribution to δVR_b	δx_p	contribution to δVR_p
hole diameter	0.004	0.00004	0.011	0.00000	0.000
coolant piping diameter	0.052	0.0001	0.005	0	0.000
coolant temperature	172	0.4	0.001	0.0	0.000
mainstream static pressure	101780	500	0.001	0	0.000
mainstream pressure differential	338	4.6	0.004	0.0	0.000
mainstream temperature	310	0.5	0.000	0.012	0.000
orifice diameter	0.028	0.00003	0.015	0	0.000
orifice static pressure	110274	500	0.020	0.008	0.000
orifice pressure differential	1370	8.6	0.020	0.0	0.000
orifice temperature	160	0.5	0.010	0.008	0.000
exit flow meter diameter	0.037	0.00001	0.004	0	0.000
exit flow meter static pressure	98337	500	0.014	0.002	0.000
exit flow meter pressure differential	166	0.72	0.012	0.04	0.001
exit flow meter temperature	192	0.2	0.003	0.008	0.000

Table 7: Bias and precision uncertainty contributions of the raw measurements to the uncertainty in coolant velocity ratio of VR = 0.5 for the 4x scale holes at VR_{ch} = 0.36

4x VRch = 0.36 VR=0.5					
	x	δx_b	contribution to δVR_b	δx_p	contribution to δVR_p
hole diameter	0.0018375	0.00004	0.024	0.00000	0.000
coolant piping diameter	0.040	0.0001	0.000	0	0.000
coolant temperature	208	0.4	0.001	0.0	0.000
mainstream static pressure	101780	500	0.001	0	0.000
mainstream pressure differential	1602	4.6	0.001	0.0	0.000
mainstream temperature	311	0.5	0.000	0.015	0.000
orifice diameter	0.025	0.00003	0.013	0	0.000
orifice static pressure	103571	500	0.007	0.001	0.000
orifice pressure differential	182	0.5	0.007	0.0	0.000
orifice temperature	180	0.5	0.006	0.011	0.000
exit flow meter diameter	0.025	0.00001	0.004	0	0.000
exit flow meter static pressure	97245	500	0.010	0.004	0.000
exit flow meter pressure differential	200	5.7	0.058	0.04	0.000
exit flow meter temperature	247	0.2	0.002	0.011	0.000

Table 8: Bias and precision uncertainty contributions of the raw measurements to the uncertainty in coolant velocity ratio of VR = 0.5 for the 4x scale holes at Re_{ch} = 57,000

4x Rech = 57,000 VR=0.5					
	x	δx_b	contribution to δVR_b	δx_p	contribution to δVR_p
hole diameter	0.0018375	0.00004	0.025	0.00000	0.000
coolant piping diameter	0.040	0.0001	0.001	0	0.000
coolant temperature	205	0.4	0.001	0.0	0.000
mainstream static pressure	101780	500	0.001	0	0.000
mainstream pressure differential	1592	4.6	0.001	0.0	0.000
mainstream temperature	311	0.5	0.000	0.017	0.000
orifice diameter	0.025	0.00003	0.020	0	0.000
orifice static pressure	104501	500	0.039	0.001	0.000
orifice pressure differential	455	5.0	0.039	0.0	0.000
orifice temperature	185	0.5	0.010	0.011	0.000
exit flow meter diameter	0.025	0.00001	0.006	0	0.000
exit flow meter static pressure	97656	500	0.017	0.04	0.000
exit flow meter pressure differential	517	0.72	0.005	0.03	0.000
exit flow meter temperature	232	0.2	0.003	0.01	0.000

All testing conditions using both scaled models showed in-test and test-to-test repeatability within uncertainty. To confirm in-test repeatability, an image was taken at the beginning of an experiment at a set of conditions and then a second image was taken at those same conditions at the end of the experiment. Laterally averaged plots of two such images are shown in Figure 37 for the 4x scale holes at a VR = 1.1. The curves agreed within $\eta \pm 0.001$, which was well within the uncertainty in adiabatic effectiveness of the 4x scale holes. The data in Figure 37 was not adjusted for any of the corrections, but both profiles would be corrected by the same amount, so the comparison was still valid. To verify test-to-test repeatability, the same conditions were run several days apart to ensure that the entire testing procedure was repeatable. Laterally averaged profiles for all three coolant velocity ratios for the 4x scale holes at VR_{ch} = 0.36 are shown in Figure 38. The repeat tests at all three coolant velocity ratios showed the same trends as the original test and the curves agreed within $\eta \pm 0.004$, except the VR = 0.5 cases which agreed within 0.008. This disagreement was due to the differences in coolant velocity ratios between the experiments due to operator error. This agreement for test-to-test repeatability, except for the VR = 0.5 case, was also within the uncertainty in adiabatic effectiveness.

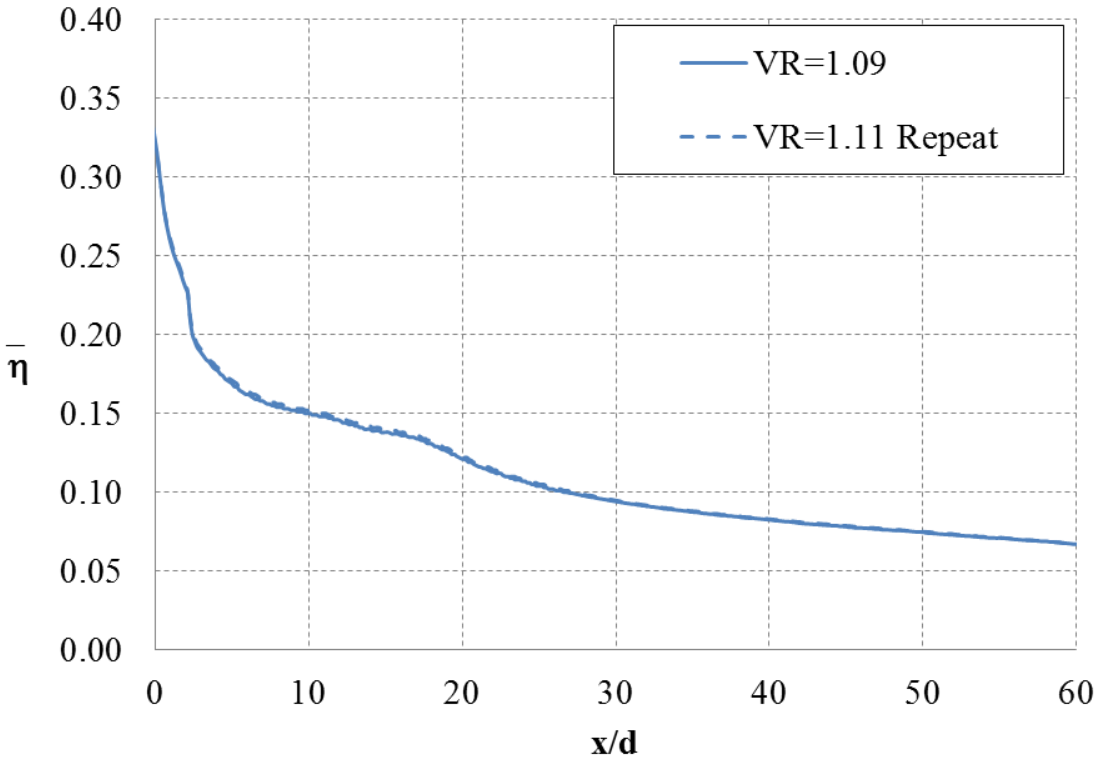

Figure 37: In-test repeatability at VR = 1.1 for the 4x scale holes at VR_{ch} = 0.36 Note: data is uncorrected

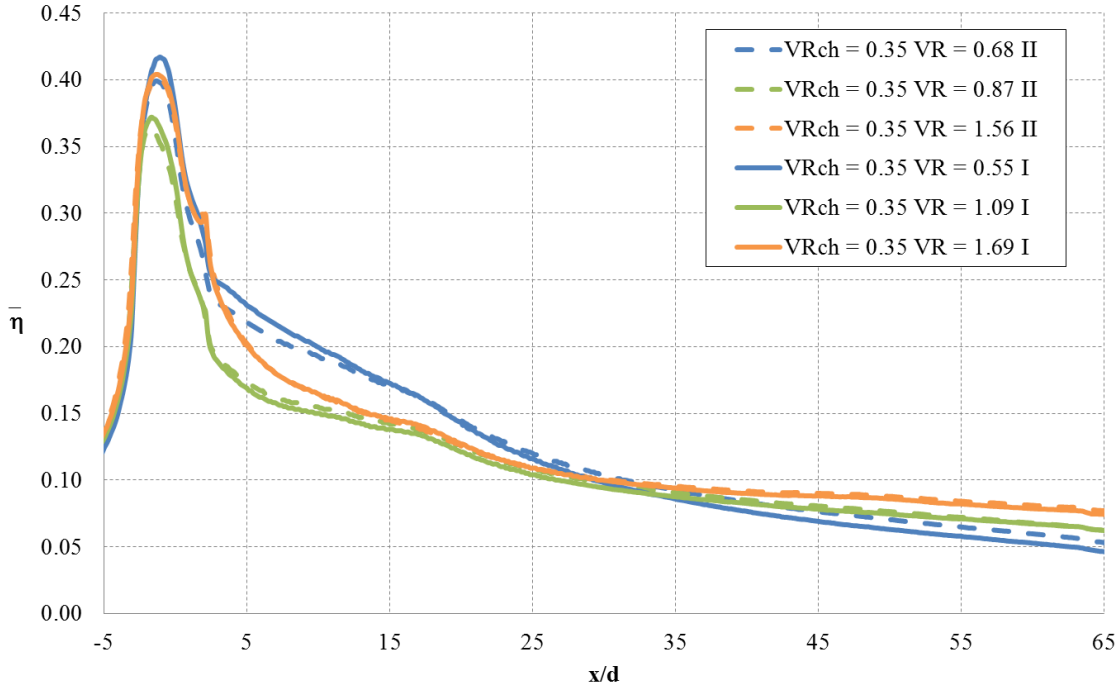

Figure 38: Test-to-test repeatability for the 4x scale holes at VR_{ch} = 0.36 Note: data is uncorrected

Results

The purpose of this study was to study the effects of crossflow channel parameters, channel Reynolds number and channel velocity ratio, on the performance of shaped cooling holes. Particular attention was given to matching the operational parameters between experiments to isolate the effects of the channel parameter. Table 1 lists the operational parameters for the four experiments compared in this study. For reference, data from a plenum fed experiment, labeled Test 1, was first compared to the channel fed results. Test 2 and 3 were compared to show the effect of channel Reynolds number and test 2 and 4 were compared to show the effect of channel velocity ratio. As previously discussed, the mainstream Mach number and density ratio were not held constant between experiments. A study by Anderson et al. [18] found that this low range of Mach numbers had a negligible effect on shaped hole performance. Although, density ratio does affect the performance of film cooling, a second study by Anderson et al. [19] revealed that the laterally averaged adiabatic effectiveness of shaped holes scaled most appropriately with coolant velocity ratio. For this study, a density ratio correction factor was developed and applied to the 4x scale data so that it was comparable with the 8x scale data at $DR = 1.8$.

Laterally averaged plots of two channel conditions compared to plenum fed holes are shown for all three coolant velocity ratios in Figure 39. At the lowest coolant velocity ratio of $VR = 0.5$, the effect of crossflow was minimal. The higher channel Reynolds number case consistently had lower effectiveness than the plenum case by approximately 30 %. The lower channel Reynolds number case upstream of $x/d = 15$ showed a 15 % decrease in effectiveness compared to the plenum fed holes, but at about $x/d = 15$, the plenum and lower channel Reynolds number case had the same effectiveness. At $VR =$

1.1, there was a distinct difference between the plenum fed and crossflow fed cases. The performance of the shaped holes was reduced by 40 % when fed by crossflow for both channel Reynolds number conditions. At the highest coolant velocity ratio, VR = 1.7, the lower channel Reynolds number case had similar effectiveness to the plenum fed holes near the coolant holes. The higher channel Reynolds number condition showed degraded performance relative to the plenum case for the entire downstream region. After x/d = 10, both the higher and lower channel Reynolds number cases showed a 30 % reduction in effectiveness relative to the plenum case. The result that crossflow reduces the effectiveness of shaped film cooling holes compared with plenum fed holes is consistent with the findings of previous studies [6] and [9].

The effect of channel Reynolds number, comparing tests 2 and 4 from Table 1, on laterally averaged effectiveness at all coolant velocity ratios is shown in Figure 40. For all conditions, the effectiveness directly downstream of the cooling holes was relatively high and decreased as the jet moved downstream. At the highest coolant velocity ratio VR = 1.7, downstream of x/d = 10 the curves converged showing that there was no effect of channel Reynolds number. Upstream of x/d = 10, a lower channel Reynolds number resulted in higher effectiveness values of up to 30 % near the coolant holes. At the lowest coolant velocity ratio VR = 0.5, a lower channel Reynolds number resulted in higher effectiveness values by 15 % over the entire downstream region. At the middle coolant velocity ratio VR = 1.1 there was a switch in the trend – increasing the channel Reynolds number resulted in an increase in effectiveness of 15 %.

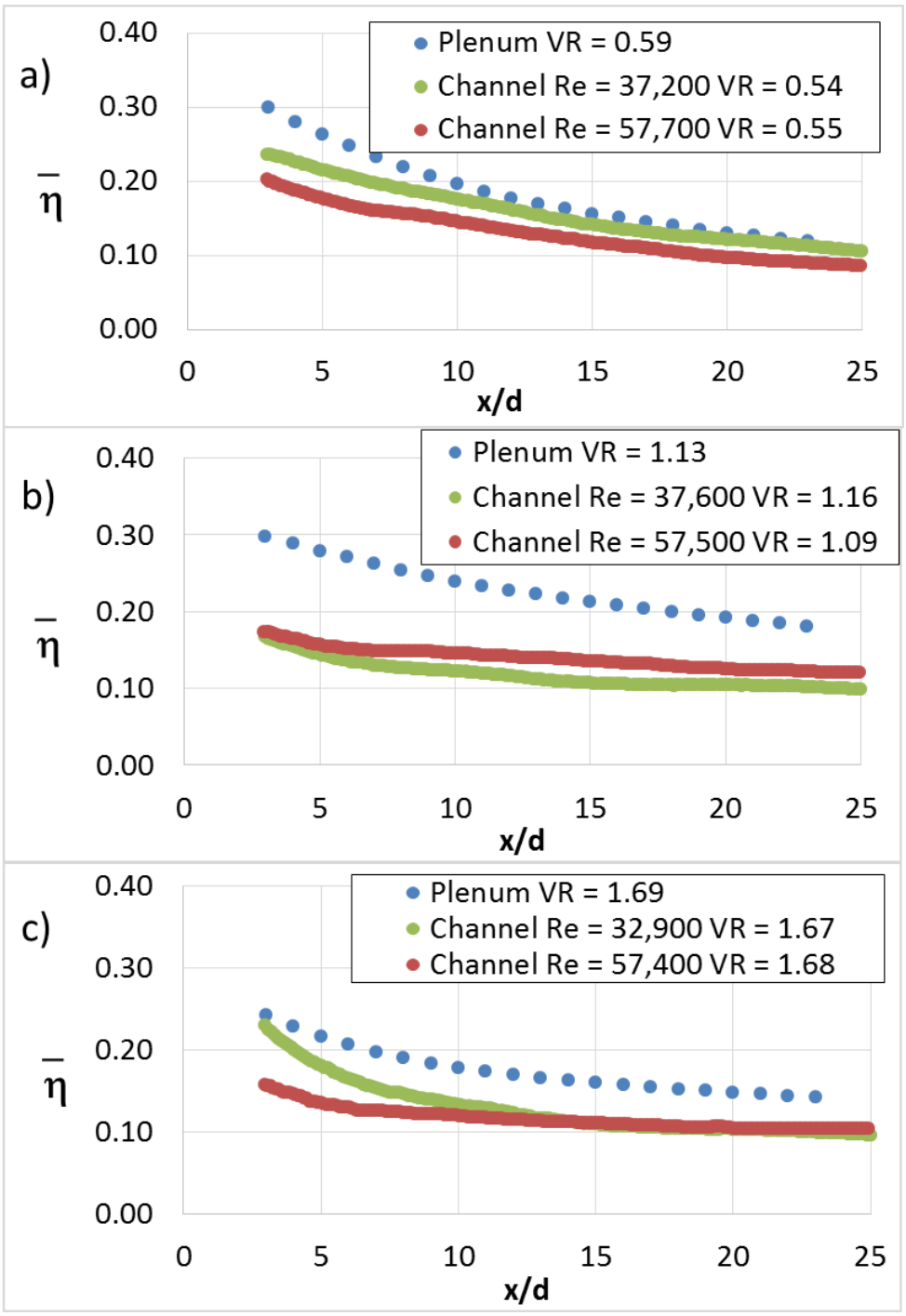

Figure 39: Laterally averaged adiabatic effectiveness comparing plenum fed holes to channel fed holes at Re_{ch} = 57,000 and 36,000 at (a) VR = 0.5 (b) VR = 1.1 and (c) VR = 1.7

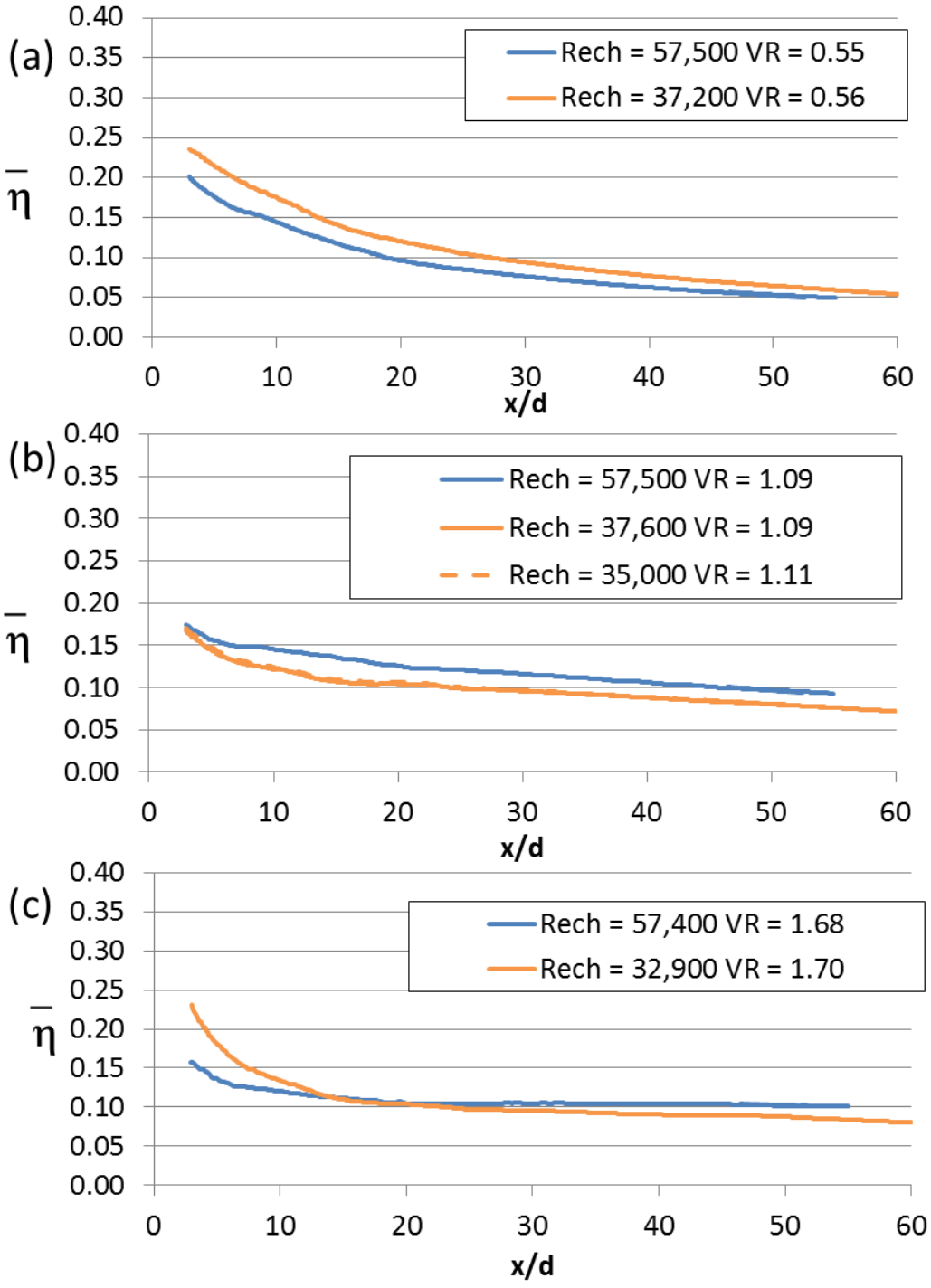

Figure 40: Laterally averaged adiabatic effectiveness comparing Re_{ch} = 57,000 and 36,000 at (a) VR = 0.5 (b) VR = 1.1 and (c) VR = 1.7

Contour plots of adiabatic effectiveness showing the spatial distribution of coolant for the channel Reynolds number comparisons are presented in Figure 41 for all three coolant velocity ratios. For all the contour plots, directly downstream of the cooling hole was the highest effectiveness and as the jet moved downstream, the jet spread laterally and had decreased effectiveness at the surface. At VR = 0.5, the lower channel Reynolds number resulted in a wider coolant distribution that extended farther downstream than the higher channel Reynolds number of Re_{ch} = 57,000. For the higher channel Reynolds number case, the coolant appeared displaced to one side at the hole exit, suggesting that the coolant jet did not fully expand in the diffuser. At VR = 1.1, the coolant distributions had similar widths at both channel Reynolds numbers, but the Re_{ch} = 57,000 distribution had higher effectiveness farther downstream. For the VR = 1.7 case, the lower channel Reynolds number contour plot, taken with the 4x scale test coupon, showed a large effect due to the presence of CPVC near the cooling holes, larger than the effect seen at the other two coolant velocity ratios. Ignoring the area upstream of x/d = 3 affected by conduction through the CPVC, the lower channel Reynolds number case had a wider distribution of coolant up to x/d = 10. Downstream of x/d = 10, the jets had very similar contours.

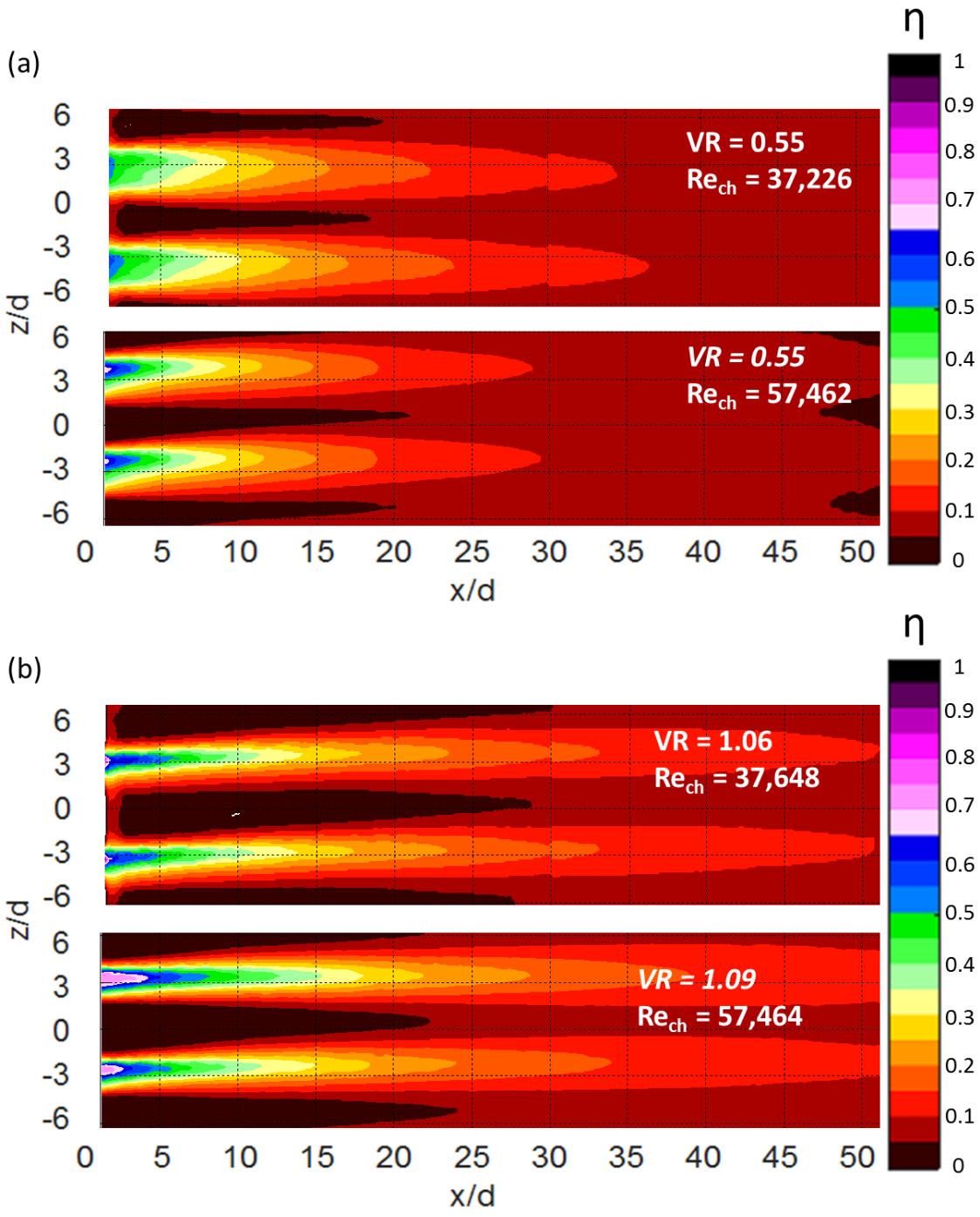
(a)
η
VR = 0.55
Re_ch = 37,226
VR = 0.55
Re_ch = 57,462
z/d
x/d
(b)
η
VR = 1.06
Re_ch = 37,648
VR = 1.09
Re_ch = 57,464
z/d
x/d

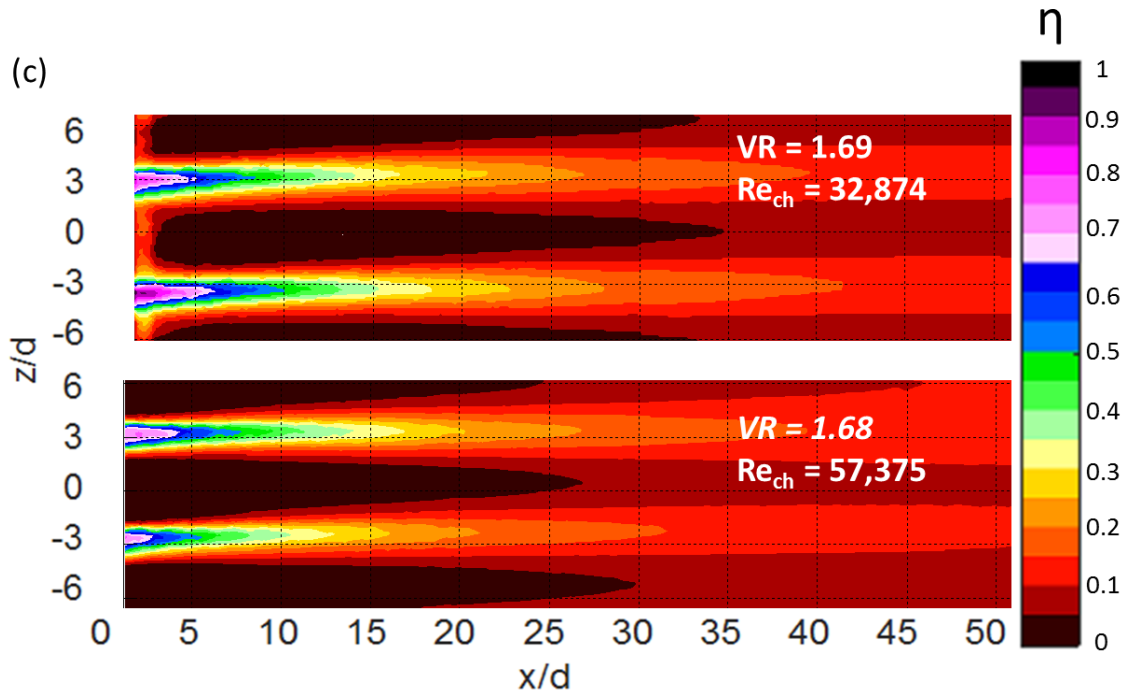

Figure 41: Contour plots of adiabatic effectiveness comparing Re_{ch} = 57,000 and 36,000 at (a) VR = 0.5 (b) VR = 1.1 and (c) VR = 1.7

Lateral profiles of adiabatic effectiveness at x/d = 10 comparing effects of channel Reynolds number are shown in Figure 42. The peaks of the lateral profiles show the location of the jet centerline and the valleys of the profiles show the between jet regions. At VR = 0.5, channel Reynolds number had minimal effects on the peak or valley effectiveness. However, a lower channel Reynolds number resulted in wider jets. Looking at the width of the jets at an arbitrary effectiveness of η = 0.20, the lower channel Reynolds number profile covered a larger z/d span than the higher channel Reynolds number profile. At VR =1.1, there was some hole-to-hole variation, but on the whole, a higher channel Reynolds number resulted in higher peak effectiveness by about 15 %. Channel Reynolds number at VR = 1.1 had minimal effect on the width of the jets.

At VR = 1.7, there was some hole-to-hole variation, but overall a higher channel Reynolds number caused a decrease in peak effectiveness by 12 %. At this velocity ratio, there was a minimal effect of channel Reynolds number on the width of the jets. To study how the jet profiles evolved downstream, Figure 43 presents lateral profiles of adiabatic effectiveness at x/d = 30. At VR = 0.5, both lateral profiles had similar shapes showing that the jets had similar widths. However, the profiles for the lower channel Reynolds number case was shifted upwards, with the lower channel Reynolds number having better peak effectiveness by $\Delta\eta$ = 0.025 and having better jet-to-jet interaction shown by the higher valley effectiveness. At VR = 1.1, despite the small jet-to-jet variability, the jet profiles had similar shape, but the higher channel Reynolds number had better peak and valley effectiveness by about $\Delta\eta$ = 0.02. At the highest coolant velocity ratio VR = 1.7, there was some jet-to-jet variability, but the jet profiles again had similar shape. A higher channel Reynolds number resulted in more jet-to-jet interaction, indicated by the higher effectiveness of the valleys, but reduced peak effectiveness, which had opposing consequences on laterally averaged effectiveness and resulted in similar laterally averaged effectiveness for the two cases downstream.

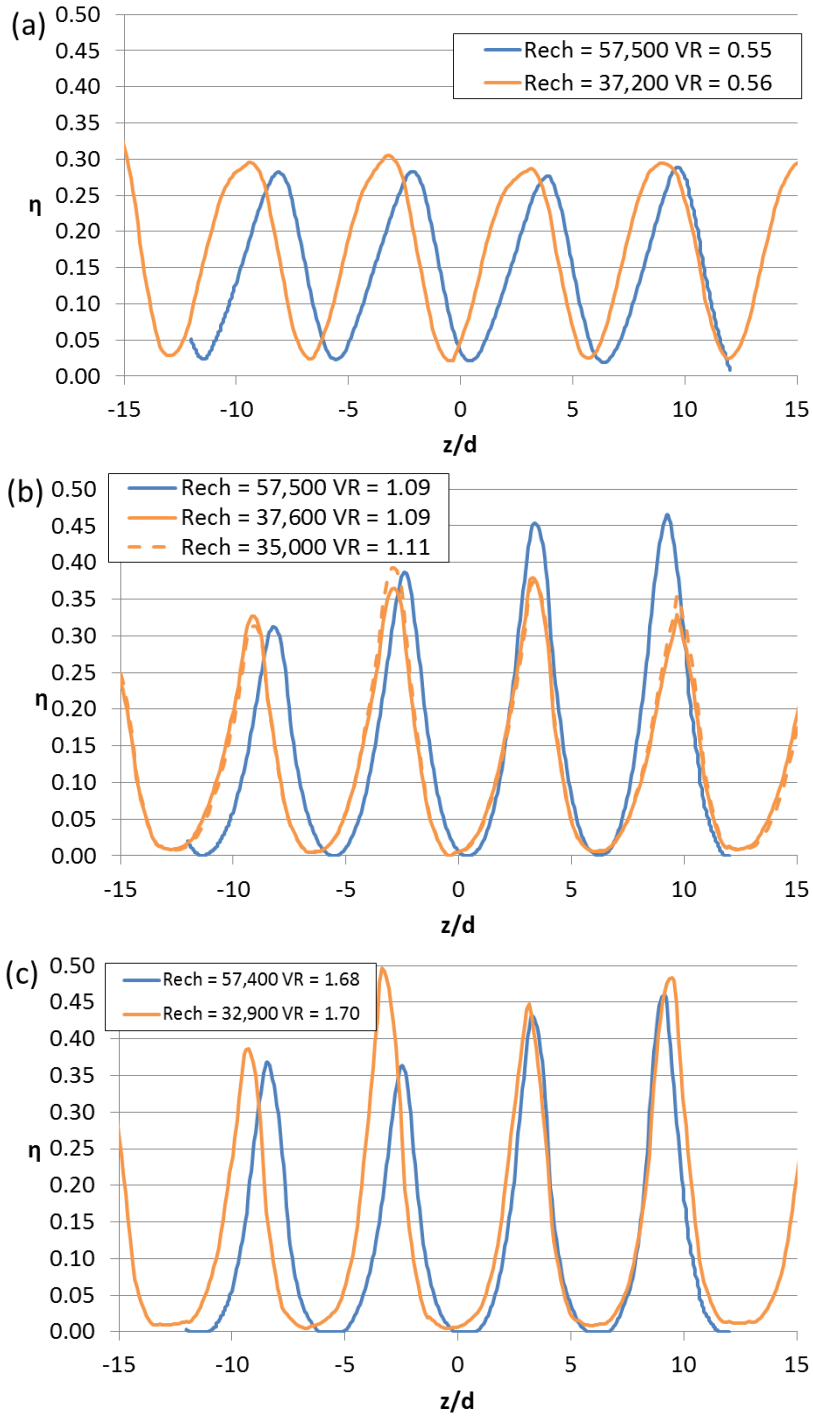

Figure 42: Lateral profiles of adiabatic effectiveness comparing Re_{ch} = 57,000 and 36,000 at x/d = 10 for (a) VR = 0.5 (b) VR = 1.1 and (c) VR = 1.7

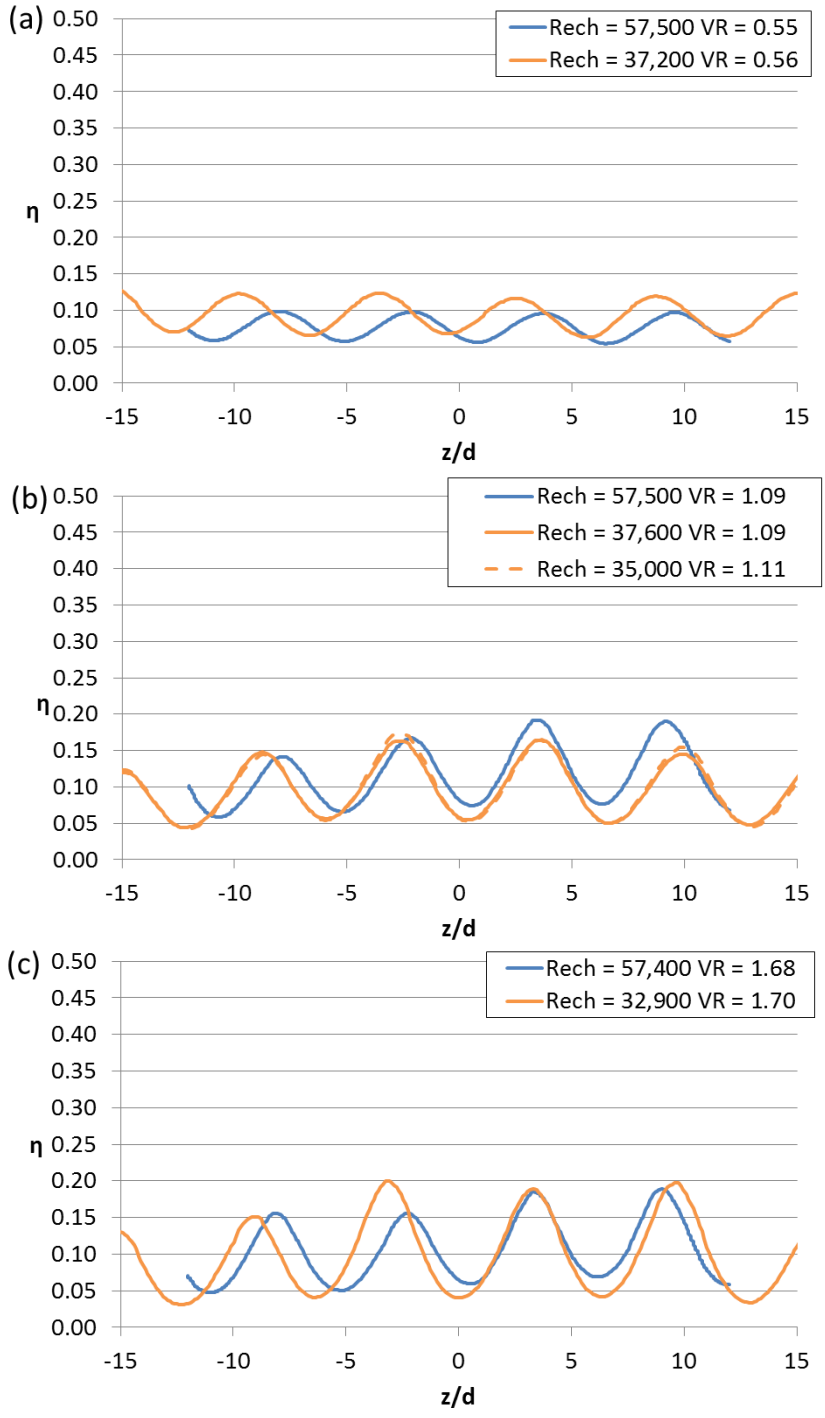

Figure 43: Lateral profiles of adiabatic effectiveness comparing Re_{ch} = 57,000 and 36,000 at x/d = 30 for (a) VR = 0.5 (b) VR = 1.1 and (c) VR = 1.7

To examine the effect of channel velocity ratio, the laterally averaged effectiveness of tests 2 and 4 from Table 1 are compared in Figure 44. For all conditions, the laterally averaged effectiveness was relatively high directly downstream of the hole exit and decreased as the jet continued downstream. At VR = 0.5, the lower channel velocity ratio of VR_{ch} = 0.36 had 25 % higher effectiveness than the higher channel velocity ratio. At VR = 1.7, the lower channel velocity ratio again had higher effectiveness by 12 % near the coolant hole and by 35 % downstream of x/d = 5. At the middle velocity ratio, the opposite trend was found with a higher channel velocity ratio yielding higher effectiveness up to 20 % near the cooling holes, but yielding no effect downstream of x/d = 45.

Contour plots showing the effect of channel velocity ratio are shown in Figure 45. At VR = 0.5, both channel velocity ratios had similar coolant distribution widths near the cooling holes. A lower channel velocity ratio, however, resulted in extended effectiveness downstream and better jet interaction. It is interesting to note that the jet profiles of the VR_{ch} = 0.63 case were skewed in the negative z/d direction while the jet profiles of all the other tested conditions were skewed in the positive z/d direction. This unusual skewing might have been due to the exceptionally low velocity through the coolant holes relative to the velocity through the coolant channel, U_c/U_{ch} or VR/VR_{ch} = 0.86. This case was the only case where VR/VR_{ch} was less than one. A high velocity through the coolant channel would cause a large separation region at the cooling hole inlet and a low velocity through the coolant hole relative to the channel might allow the helical motion through the hole to complete more rotations causing an oppositely skewed profile. The contours at VR = 1.1 showed that a higher channel velocity ratio resulted in a wider distribution of coolant that was sustained downstream. At VR = 1.7, the coolant distributions of the two cases had

similar widths, but a lower channel velocity ratio resulted in better sustained effectiveness downstream and better jet interaction.

The effect of channel velocity ratio can be further shown by comparing lateral profiles of adiabatic effectiveness at x/d = 10 for all coolant velocity ratios in Figure 46. At VR = 0.5, a VR_{ch} = 0.36 resulted in significantly higher peak effectiveness by 35 %. The unusual jet skewing was clearly visible in the lateral profiles where the peaks of the higher channel velocity ratio were pointed in the negative z/d direction while the lower channel velocity ratio peaks were slightly pointed in the positive z/d direction. At VR = 1.1, there was some hole-to-hole variation for the lower channel velocity ratio case. Due to this variation, it was difficult to conclude the effect of channel velocity ratio on peak effectiveness, but looking at the width of the profiles at η = 0.2, a higher channel velocity ratio resulted in a wider jet profile. At VR = 1.7, there was some hole-to-hole variation for both cases. Despite this variation, it was clear that a lower channel velocity ratio resulted in higher peak effectiveness by 35 %. Figure 47 presents a comparison of lateral profiles at x/d = 30 looking at the effect of channel velocity ratio. At the lowest coolant velocity ratio VR = 0.5, the two profiles had similar shape, but the VR_{ch} = 0.36 case was shifted upwards resulting in higher 25 % peak and valley effectiveness. At VR = 1.1, there was some hole-to-hole variation for the lower channel velocity ratio case, so no comparisons of peak or valley effectiveness were available. However, the widths of the jet profiles for both cases were very similar. At VR = 1.7, there was some hole-to-hole variation for both cases, but the lower channel velocity ratio case resulting in distinctly higher peak and valley effectiveness by 30 %.

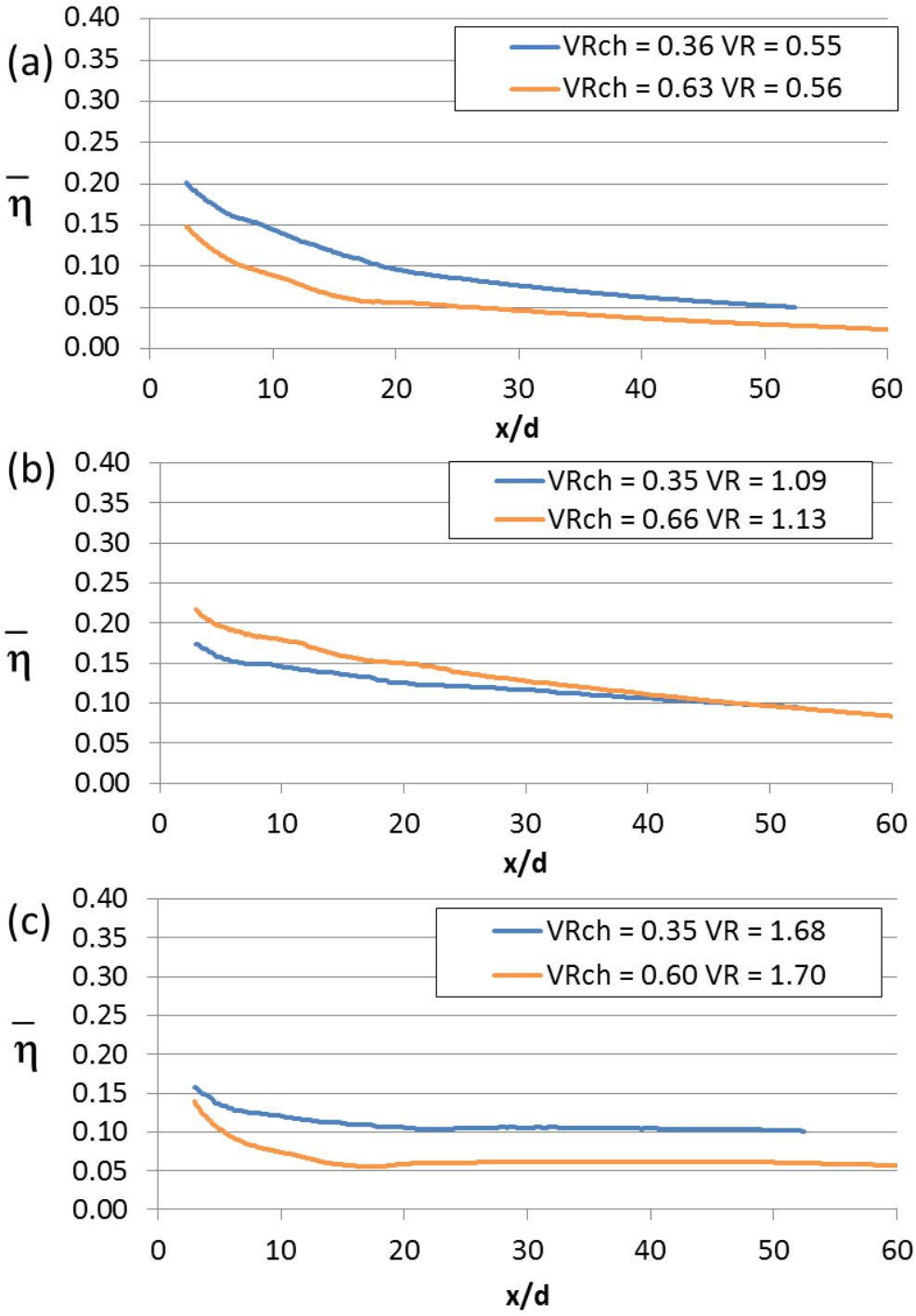

Figure 44: Laterally averaged adiabatic effectiveness comparing VR_{ch} = 0.64 and 0.35 at (a) VR = 0.5 (b) VR = 1.1 and (c) VR = 1.7

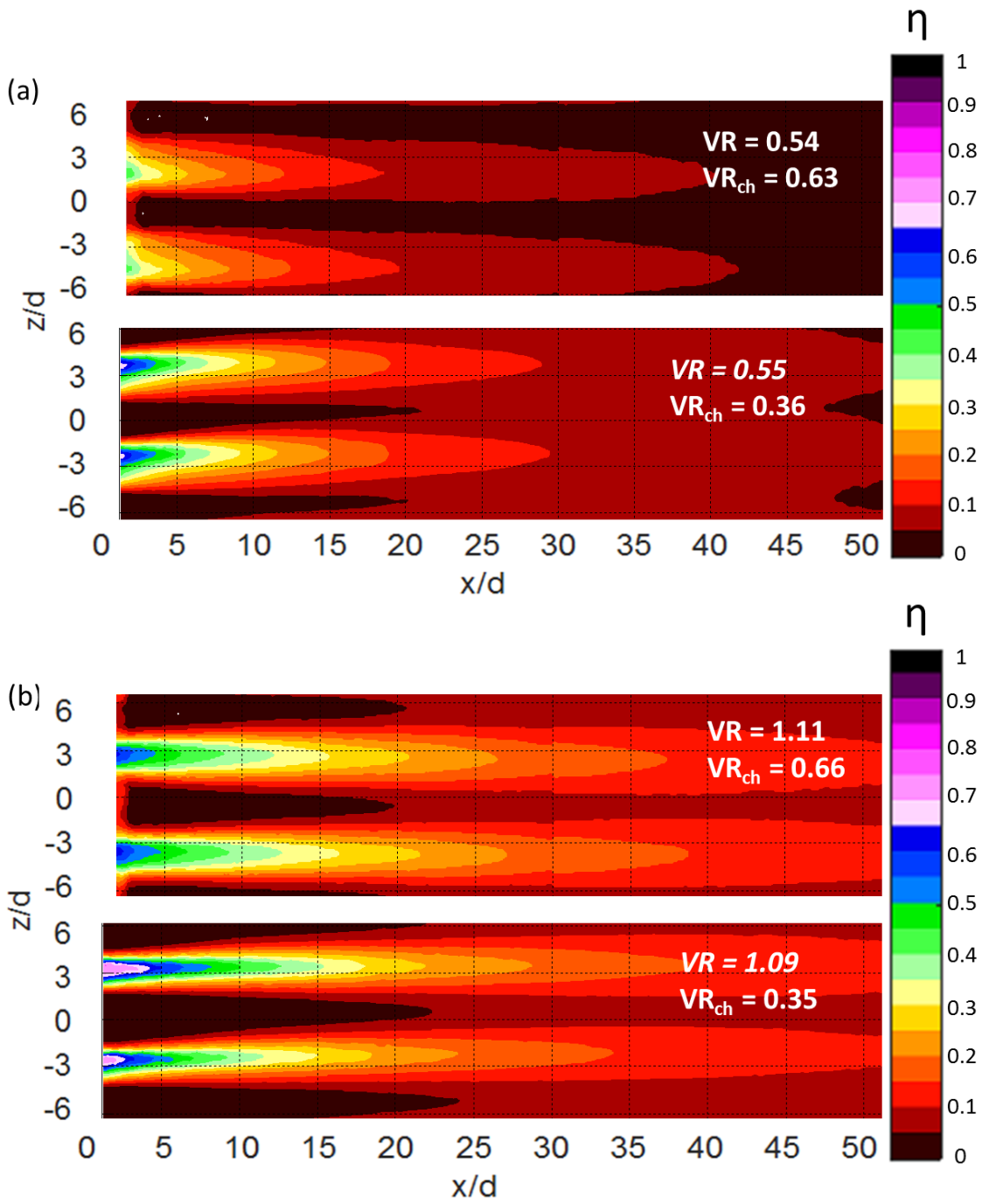
(a)
VR = 0.54
VR_ch = 0.63
VR = 0.55
VR_ch = 0.36
z/d
x/d
η
(b)
VR = 1.11
VR_ch = 0.66
VR = 1.09
VR_ch = 0.35
z/d
x/d
η

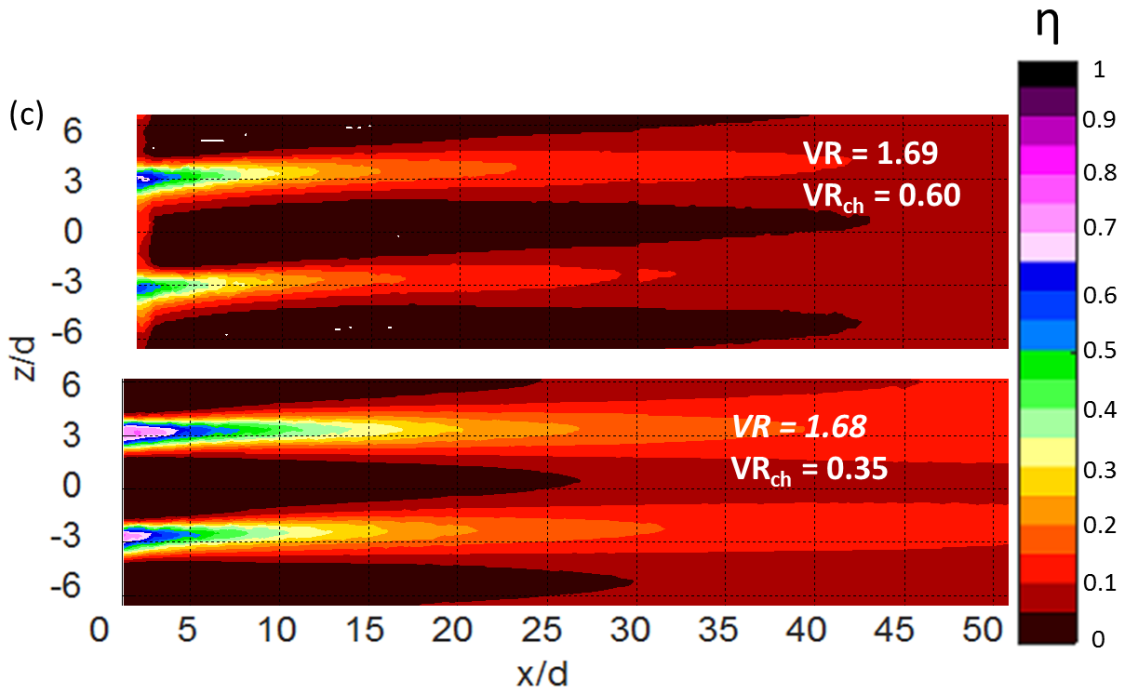

Figure 45: Contour plots of adiabatic effectiveness comparing VR_{ch} = 0.64 and 0.35 at (a) VR = 0.5 (b) VR = 1.1 and (c) VR = 1.7

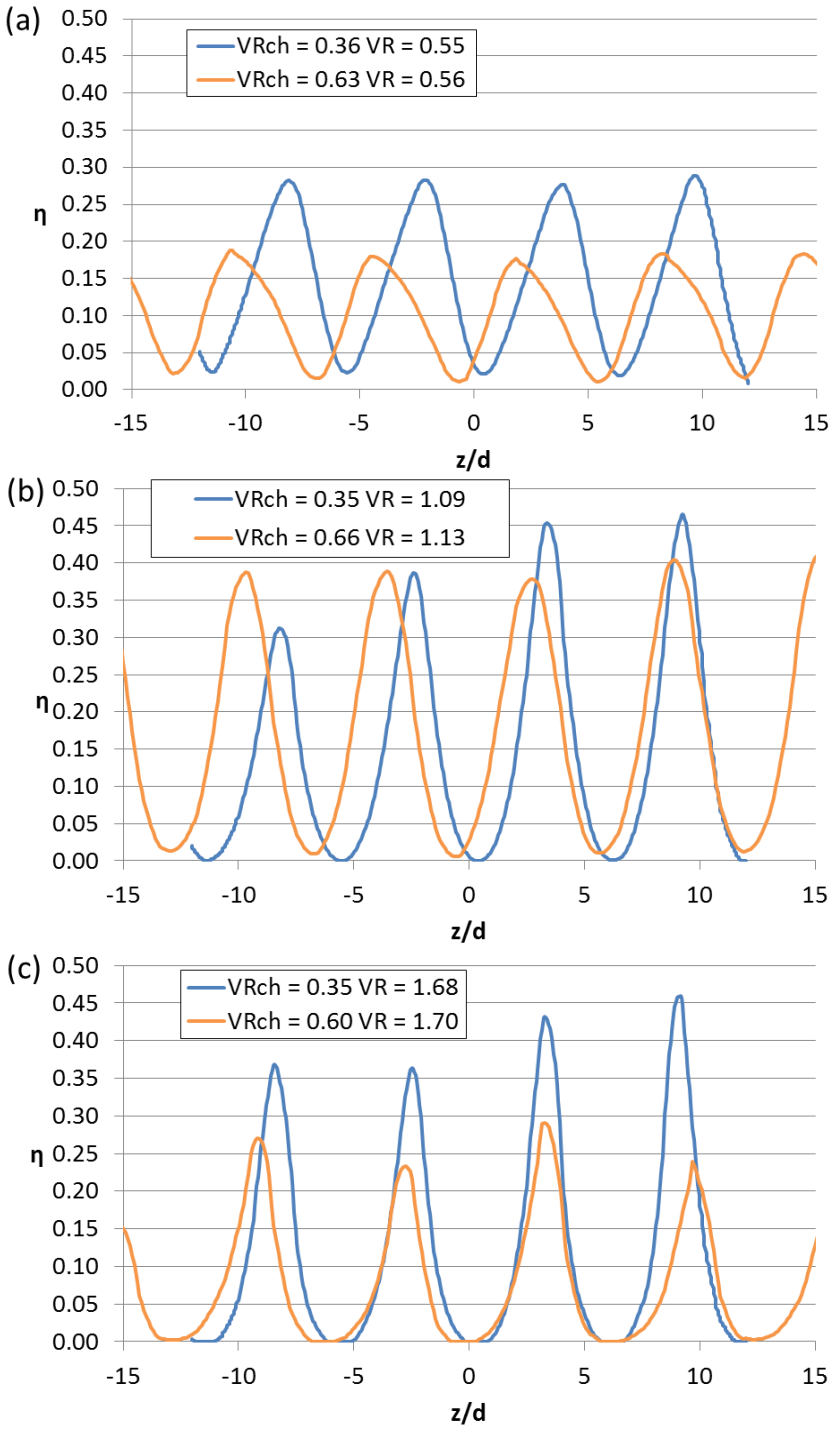

Figure 46: Lateral Profiles of adiabatic effectiveness comparing VR_{ch} = 0.64 and 0.35 at x/d = 10 for (a) VR = 0.5 (b) VR = 1.1 and (c) VR = 1.7

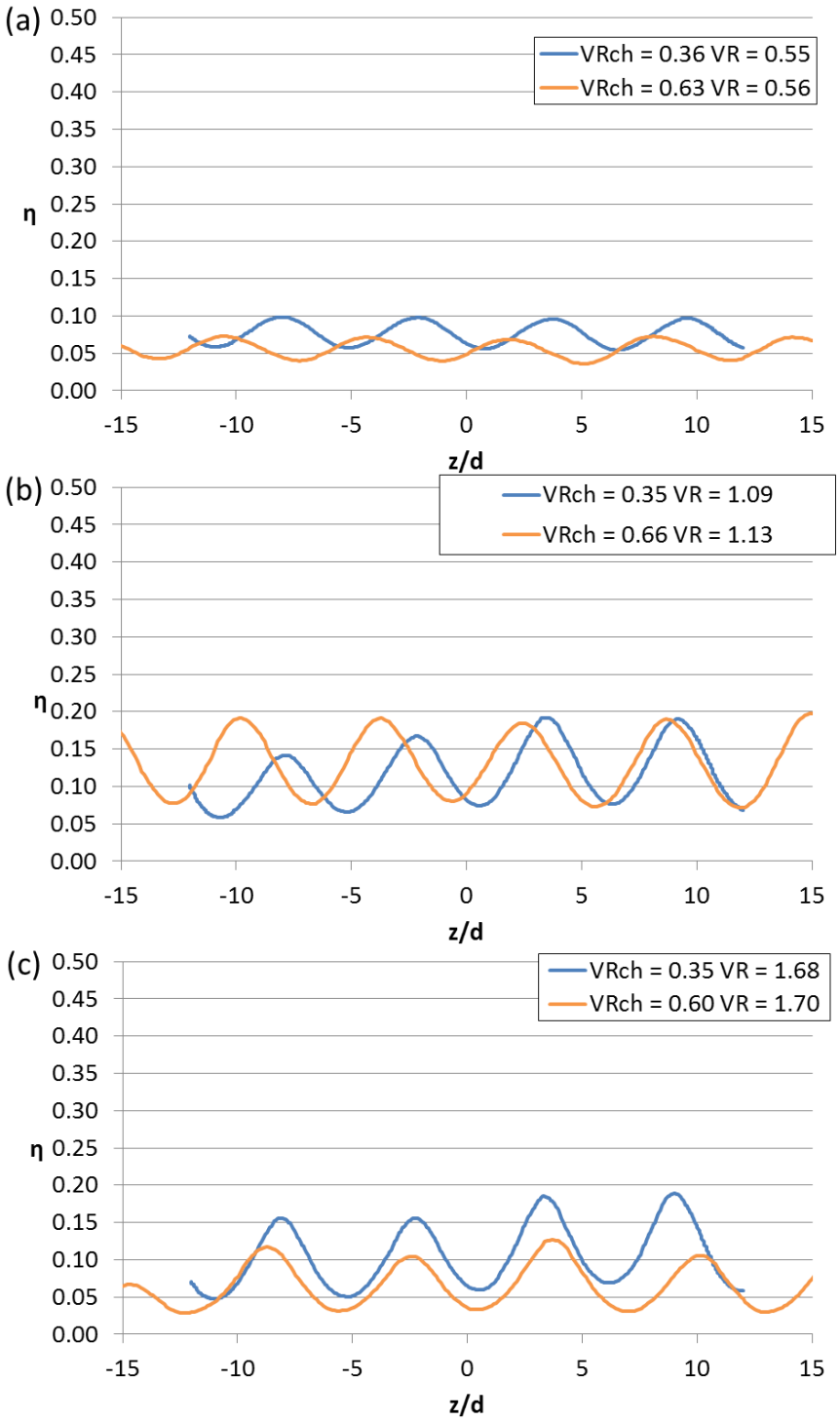

Figure 47: Lateral Profiles of adiabatic effectiveness comparing VR_{ch} = 0.64 and 0.35 at x/d = 30 for (a) VR = 0.5 (b) VR = 1.1 and (c) VR = 1.7

To further investigate the switch in the effect of both channel Reynolds number and channel velocity ratio performance at the middle coolant velocity ratio, the effectiveness for all four test conditions at x/d = 10 were plotted against coolant velocity ratio, shown in Figure 48. The conditions of Tests 1, 2, 3, and 4 are tabulated in Table 1. Comparing the trends of Tests 2 and 4 showed that increasing the channel velocity ratio resulted in a greater sensitivity to coolant velocity ratio shown by the steeper curve for Test 4. Similarly, Tests 2 and 3 showed that decreasing the channel Reynolds number resulted in a greater sensitivity to coolant velocity ratio but in the opposite direction where the effectiveness at VR = 1.1 was a minimum and not a maximum. Tests 1, 2, and 4 ratio showed the expected trend for the 7-7-7 shaped hole where the effectiveness peaked around VR = 1.1 and dropped off to either side. Test 3 showed the opposite trend where the effectiveness increased from a minimum value at VR = 1.1. A repeat of Test 3 but at different coolant velocity ratios validated the shape of the trend. Eventually, at low enough coolant velocity ratios, the effectiveness would approach zero since minimal coolant would be exiting the film cooling holes and at high enough coolant velocity ratios, the effectiveness would approach zero because the jets would begin to separate from the surface. However, at least within this range of velocity ratios, decreasing the channel velocity ratio caused this unique trend and a reversal of the effect of coolant velocity ratio on effectiveness.

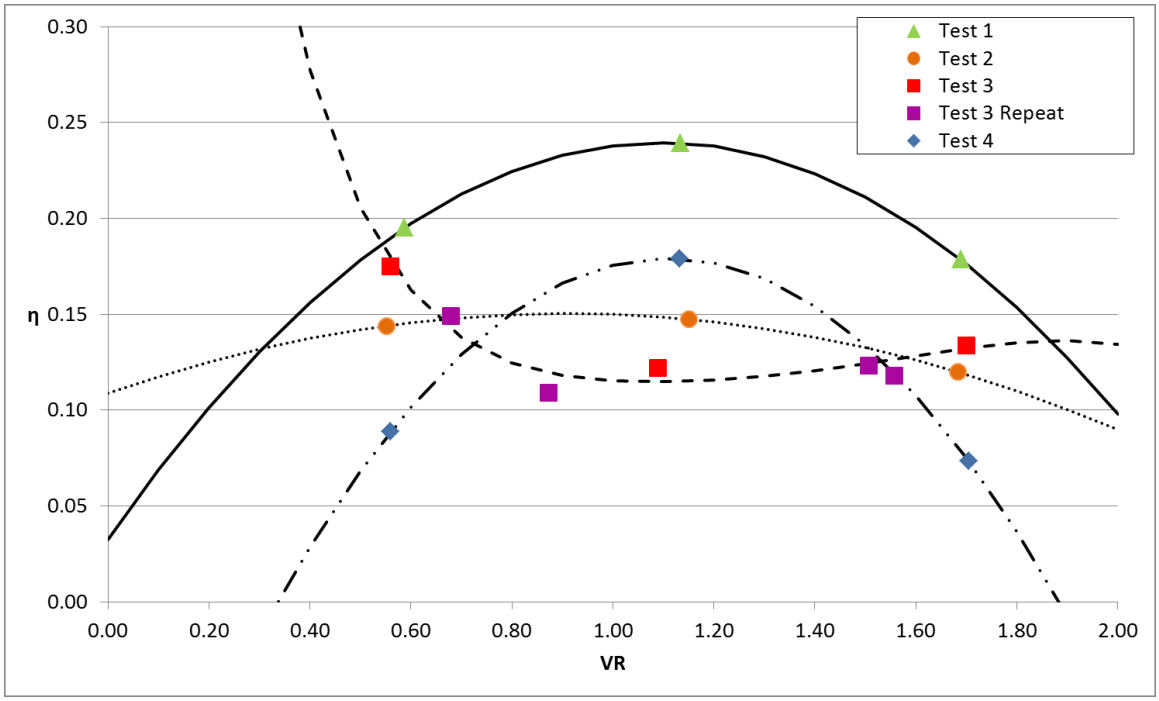

Figure 48: Adiabatic effectiveness at x/d = 10 as a function of coolant velocity ratio for the four operational conditions

Conclusions

This thesis presented a study of internal crossflow parameters, channel velocity ratio and channel Reynolds number, on the effectiveness of shaped hole film cooling. A comparison to plenum fed shaped cooling holes was also presented for reference.

Crossflow fed shaped cooling holes, compared to plenum fed shaped holes, showed a 30 - 40 % decrease in adiabatic effectiveness. There was an exception at low coolant velocity ratios where the plenum and crossflow fed cooling holes had similar performance, particularly downstream of about x/d = 10. Upstream of this position, there was a 20 % decrease in effectiveness due to crossflow. The reduced performance of internal crossflow fed holes suggested that crossflow effects at the cooling hole inlet negatively impacted the uniform distribution of coolant in the diffusing section of the shaped hole.

The effects of channel velocity ratio from VRch = 0.36 to 0.64 were examined while holding the channel Reynolds number constant at Rech = 57,000. An increase in channel velocity ratio resulted in a 30 % decrease in effectiveness at the lowest and highest coolant velocity ratios. However, at the middle velocity ratio of VR = 1.1, a higher channel velocity ratio resulted in a 10 % increase in effectiveness near the hole exits. Downstream of the hole exits, about x/d = 25, the high and low channel velocity ratios showed similar effectiveness.

The effects of channel Reynolds number from Rech = 38,000 to 57,000 were investigated while holding the channel velocity ratio constant at VRch = 0.36. At the lowest coolant velocity ratio, an increase in channel Reynolds number resulted in a 10 % decrease in effectiveness. At the highest velocity ratio, upstream of x/d = 15, an increase in channel Reynolds number resulted in a 30 % decrease in effectiveness. Downstream of

x/d = 15, there was minimal difference between the two cases. At the middle velocity ratio VR = 1.1, as with the VRch comparison, there was a swap in the trend. At VR = 1.1, an increase in channel Reynolds number resulted in an increase in effectiveness of 20 %.

Overall, channel velocity ratio had a larger effect on the performance of shaped holes than channel Reynolds number. This suggested that the separation region at the inlet of the film cooling hole and the flow formation through the cooling hole was affected more by the velocity of the coolant through the channel relative to the velocity of the coolant through the coolant hole than by the channel Reynolds number.

RECOMMENDATIONS FOR FUTURE STUDIES

The trend switch seen at the middle coolant velocity ratio of VR = 1.1 for both comparisons was unexpected and should be examined further. The channel velocity ratio and Reynolds number both perhaps had an effect on the peak effectiveness relative to coolant velocity ratio. The translation of the peak effectiveness to a different coolant velocity ratio might result in the switch seen.

As mentioned in the Introduction, there is no knowledge regarding the heat transfer coefficient augmentation for shaped holes in crossflow. In this thesis, it was assumed that the heat transfer coefficient for the experiments was the same as the heat transfer coefficient augmentation for shaped holes fed by a plenum. There is no confirmation that this was a correct assumption, and thus future experimentation on the heat transfer coefficient augmentation of shaped holes in crossflow is needed.

This thesis proposed a density ratio correction factor. Although the correction factor was determined from experimental results, these results were obtained from shaped holes fed by a plenum. To confirm that the correction factor calculated applies to shaped

holes fed by crossflow, further testing at similar conditions but at DR = 1.5 and 1.8 must be completed with data that extends beyond x/d = 25 to justify the linear trend that was applied after this position in this thesis. Lastly, additional validation of the density correction itself is necessary to determine whether a density ratio correction can be extrapolated to situations other than the conditions of the tests used to calculate the correction.

References

[1] G. Packard, "Experimentally Determined External Heat Transfer Coefficient of a Turbine Airfoil Design at Varying Incidence Angles," in *MS Thesis*, UT Austin, 2015.

[2] D. Quattrochi, "Brayton Cycle," MIT Thermodynamics and Propulsion, 6 August 2006. [Online]. Available: http://web.mit.edu/16.unified/www/SPRING/propulsion/notes/node27.html. [Accessed September 2015].

[3] W. Siddique, "Design of Internal Cooling Passages: Investigation of Thermal Performance of Serpentine Passages," in *Doctoral Thesis* , Stockholm, Sweden, Royal Institute of Technology, 2011.

[4] "What is Film Cooling?," [Online]. Available: http://www.me.umn.edu/labs/tcht/measurements/what.html. [Accessed 2015].

[5] A. Kohli and K. A. Thole, "A CFD Investigation on the Effects of Entrance Crossflow Directions to Film-Cooling Holes," in *ASME Proceedings of the 32nd National Heat Transfer Conference*, Baltimore, MD, 1997.

[6] W. Peng and P. -X. Jiang, "Experimental and Numerical Study of Film Cooling with Internal Coolant Cross-flow Effects," *Experimental Heat Transfer: A Journal of Thermal Energy Generation, Transport, Storage, and Conversion,* vol. 25, pp. 282-300, 2012.

[7] M. Gritsch, A. Schulz and S. Wittig, "Adiabatic Wall Effectiveness Measurements of Film-Cooling Holes with Expanded Exits," *Journal of Turbomachinery,* vol. 120, pp. 549-556, 1998.

[8] M. Gritsch, A. Schulz and S. Wittig, "Effect of Internal Coolant Crossflow on the Effectiveness of Shaped Film-Cooling Holes," *Journal of Turbomachinery,* vol. 125, pp. 547-554, 2003.

[9] C. Saumweber and A. Schulz, "Comparison of the Cooling Performance of Cylindrical and Fan-Shaped Cooling holes with Special Emphasis on the Effect of Internal Coolant Cross-Flow," in *Proceedings of ASME Turbo Expo 2008: Power for Land, Sea and Air*, Berlin, Germany, 2008.

[10] C. Saumweber, A. Schulz, S. Wittig and M. Gritsch, "Effects of Entrance Crossflow Directions to Film Cooling Holes," *Annals New York Academy of Sciences,* pp. 401-408, 2001.

[11] M. Gritsch, C. Saumweber, A. Schulz, S. Wittig and E. Sharp, "Effect of Internal Coolant Crossflow Orientation on the Discharge Coefficient of Shaped Film-Cooling Holes," *Journal of Turbomachinery,* vol. 122, pp. 146 - 152, 2000.

[12] P. Adami, F. Martelli, F. Montomoli and C. Saumweber, "Numerical Investigation of Internal Crossflow Film Cooling," in *ASME Turbo Expo 2002*, Amsterdam, The Netherlands, 2002.

[13] E. J. Boyd, "Parameters that Affect Shaped Hole Film Cooling Performance and the Effect of Density Ratio on Heat Transfer Coefficient Augmentation," in *Dissertation*, Austin, Texas, The University of Texas at Austin, 2014.

[14] K. Thole, M. Gritsch, A. Schulz and S. Wittig, "Flowfield Measurements for Film-Cooling Holes with Expanded Exits," *Journal of Turbomachinery,* vol. 120, pp. 327-336, 1998.

[15] R. P. Schroeder and K. A. Thole, "Adiabatic Effectiveness Measurements for a Baseline Shaped Film Cooling Hole," in *Proceedings of ASME Turbo Expo 2014: Turbine Technical Conference and Exposition*, Dusseldorf, Germany, 2014.

[16] D. L. Schmidt, B. Sen and D. G. Bogard, "Film Cooling with Compound Angle Holes: Adiabatic Effectiveness," *Journal of Turbomachinery,* vol. 118, pp. 807-813, 1996.

[17] S. R. Klavetter, "Internal Crossflow Effects on Turbine Airfoil Film Cooling Adiabatic Effectiveness with Compound Angle Round Holes," in *Thesis*, Austin, Texas, The University of Texas at Austin, 2014.

[18] J. B. Anderson, E. K. Wilkes, J. W. McClintic and D. G. Bogard, "Effects of Freestream Mach Number, Reynolds Number, and Boundary Layer Thickness on Film Cooling Effectiveness of Shaped Holes," in *Proceedings of the ASME Turbo Expo 2016: Turbine Technical Conference and Exposition* , Seoul, South Korea, 2016.

[19] J. B. Anderson, E. J. Boyd and D. G. Bogard, "Experimental Investigation of

Coolant-to-Mainstream Scaling Parameters with Cylindrical and Shaped Film Cooling Holes," in *Proceedings of the ASME Turbo Expo 2015: Turbine Technical Conference and Exposition*, Montreal, Canada, 2015.

[20] S. R. Klavetter, J. W. McClintic, D. G. Bogard, J. Dees, G. M. Laskowski and R. Briggs, "The Effect of Rib Turbulators on Film Cooling Effectiveness of Round Compound Angle Holes Fed by an Internal Cross-Flow," in *Proceedings of the ASME Turbo Expo 2015*, Montreal, Canada, 2015.

[21] J. W. McClintic, S. R. Klavetter, J. B. Anderson, J. R. Winka, D. G. Bogard, J. E. Dees, G. M. Laskowski and R. Briggs, "The Effect of Internal Cross-Flow on teh Adiabatic Effectiveness of Compound Angle Film Cooling Holes," in *Proceedings of the ASME Turbo Expo 2014*, Dusseldorf, Germany, 2014.